Marine and Petroleum Geology 115 (2020) 104241

Contents lists available at ScienceDirect

Marine and Petroleum Geology

journal homepage: www.elsevier.com/locate/marpetgeo

Structural geological interpretations from unrolled images of drill cores

Megha Chakraborty, Soumyajit Mukherjee*

Department of Earth Sciences, Indian Institute of Technology Bombay, Powai, Mumbai, 400 076, Maharashtra, India

ARTICLE INFO

Keywords:
Numerical model
3D co-ordinate geometry
Drilling
Geometric representation of geological structures
MATLAB programming
Structural geology
Applied structural geology

ABSTRACT

Structures hidden at depth can be assessed through drill cores recovered from them. A crucial part of petroleum geology study is to interpret structures from these cores collected from vertical and inclined drilling operations reaching different depths. We deduce analytically ideal structures in unrolled/unwrapped images of cylindrical drill cores. These structures are: *(i)* orthogonal and conjugate fractures, *(ii)* single generation periodic folds and type-1 and type-2 superposed folds, *(iii)* listric faults and *(iv)* different types of angular unconformities. The sinuous curves as found in unrolled images are not always characteristic of the structures. Therefore accurate identification of structures would require additional information, such as the drill core itself.

1. Introduction

"Accurate orientation of fractures in drill cores can be critical for understanding neotectonic stress, structural history and reservoir productivity …" Paulsen et al. (2002)

Despite several drilling programs being undertaken worldwide, deciphering structural geology from cores have not received the due attention that it should (Shigematsu et al., 2014). This is true even though *(i)* works have been undertaken in bits and pieces by several organizations worldwide; and *(ii)* image logs have become popular since 1980s (Liu, 2017). Oriented cores measured in goniometers to find out the attitude of the planes that intersect the cores (e.g., Fig. 5 of Zimmer, 1963) is one such example. Lau (1983) presents a method of deducing attitudes of planes that intersect cores using independent methods of stereogram, spherical trigonometry and analytical geometry. Johnson (1985) works out how refolded folds will look like in cores in terms of stereoplots of the deduced planes (also see Laing, 1977). Sikorski (1991) plots strike and dip against borehole length and identified specific domains for a particular core from the Lac du Bonnet batholith (Canada). Computer-based rapid data generation from cores have been possible for several decades (Hinman, 1993). Paulsen et al. (2002) correlate while-core scan and borehole-wall images for a robust interpretation of structural data. Scott and Berry (2004) use Monte Carlo simulation to study structural data from axially-oriented cores. Scott and Selley (2004) present the detailed method of finding out the attitude of fold axes from drill cores. Yeh et al. (2007) demonstrate how to interpret faults from core data. Quiniou et al. (2007) in their Fig. 3 present raw image of cores that gives only a portion of the plane-core intersection scenario. Blenkinsop and Doyle (2010) demonstrate how to interpret S–C and S–C′ fabric from the drill cores using the half core method. Zosel (2015) demonstrate how pixel of images to be modified when unrolling of an image is to be done. How to deduce attitude data of planes from their occurrences in cores is well established (e.g., Figs. 4.13 and 4.14 of Abzalov, 2016). Marjoribanks (2012) provides several sketches of drill cores that cut across planar surfaces (his Fig. 7.3), faults (his Fig. 7.4), lineations (his Fig. 7.5), and folds (his Fig. 7.7 and 7.8). But none of these works present explicitly the unrolled image of the cylindrical drill cores demonstrating different structures.

Such unrolled images can be obtained from different types of image logs. Dipmeter logs are the "ancestors" of image logs, which came into existence since 1930s (Cornet, 2013). Al-Sit (2015) reviews borehole imaging techniques that enhances the line of intersection between the drill core and the geological structures. Correct interpretation of natural geological structures can constrain the stress directions, which is a valuable input in petroleum geology (e.g., Morin, 2017).

In the unrolled images generated from cores, one can find different geometries of sinuous curves of planes (Fig. 2 in Tiwari et al., 2017, Fig. 5(a) of Dasgupta et al., 2019). Hence there is a need to understand the geometry of these curves in more detail for their more accurate interpretations by geoscientists and petroleum engineers. This would help in better 3D structural geological interpretation of the sub-surface. From such representation of drill cores, a novice can quickly make out the first order structures.

How few structures of specific geometries would manifest in the unrolled images of cores is, therefore, the subject of this article. ***A.*** We

* Corresponding author.
E-mail addresses: soumyajitm@gmail.com, smukherjee@iitb.ac.in (S. Mukherjee).

https://doi.org/10.1016/j.marpetgeo.2020.104241
Received 6 August 2019; Received in revised form 12 January 2020; Accepted 13 January 2020
Available online 21 January 2020

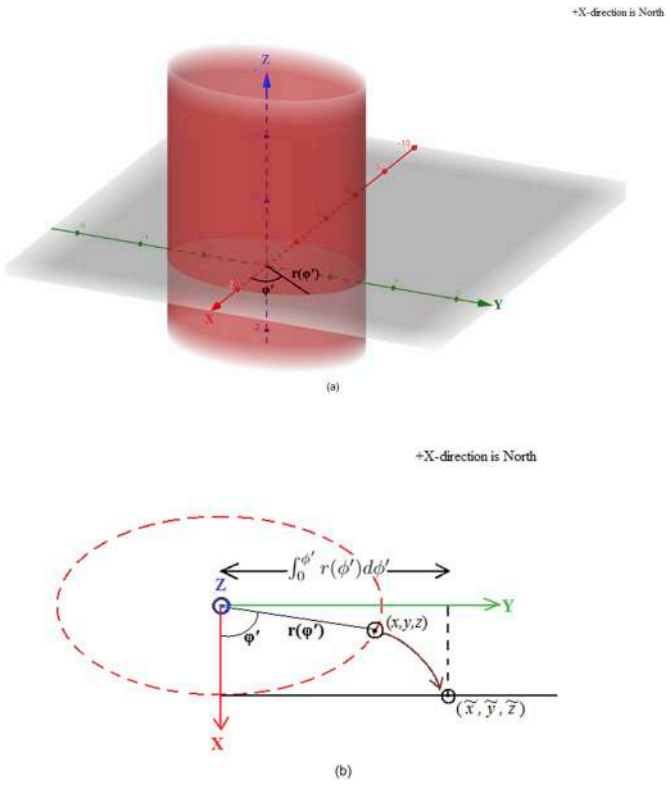

Fig. 1. (a): Choice of coordinate system in reference to a horizontal plane and a vertical drill core with an elliptical cross-section. Subsection 2.1 defines φ' and $r(\varphi')$. See Section 2.1 for details. **(b):** Plan view showing the XY-plane of the elliptical cross-section. Subsection 2.2 explains symbols. See Section 2.2 for details.

first deduce how a dipping plane that got cut by a cylindrical drill core with an elliptical cross-section would ideally look like in an unrolled image. Then, the geotechnical case of cylindrical drill core with circular cross-section is considered. ***B.*** The following structures are presented in ideal cases in unrolled images: *(i)* orthogonal fractures (subsection 2.5.1.1) and conjugate fractures (subsection 2.5.1.2); *(ii)* single generation periodic folds (subsection 2.5.2.1) and type-1 and 2 superposed folds (subsection 2.5.2.2); and *(iii)* ideal listric faults (subsection 2.5.3). 3D diagrams are prepared in this article using the free online software GeoGebra 3D Calculator (www.geogebra.org), Version 6.0.562.0.

2. The model

2.1. Intersection between a cylindrical drill core and a plane

Consider a long cylinder with an elliptical cross-section (Fig. 1(a)). Let φ' be the angle that the radial vector makes with the X-axis at any point on the curved surface on the equatorial plane. Therefore, the parametric equation of the cylinder is:

$$x = r(\varphi')\cos\varphi' \tag{1}$$

$$y = r(\varphi')\sin\varphi' \tag{2}$$

where $r(\varphi')$ is the radial distance from the Z-axis. Taking the equation of the cross-section:

$$\frac{x^2}{\alpha^2} + \frac{y^2}{\beta^2} = 1 \tag{3}$$

Here, α and β are the semi-minor and the semi-major axes, respectively. Combining eqns (1)–(3):

$$\frac{r^2\cos^2\varphi'}{\alpha^2} + \frac{r^2\sin^2\varphi'}{\beta^2} = 1 \tag{4}$$

$$r^2 = \frac{\alpha^2\beta^2}{\beta^2\cos^2\varphi' + a^2\sin^2\varphi'} \tag{5}$$

$$\therefore r(\varphi') = \frac{\alpha\beta}{[\beta^2\cos^2\varphi' + \alpha^2\sin^2\varphi']^{1/2}} \tag{6}$$

Consider a plane passing through the origin:

$$ax + by + cz = 0 \tag{7}$$

To find the equation of the line of intersection between the cylinder and the plane, eqns (1) and (2) are substituted into 7:

$$z = -\frac{ar(\varphi')\cos\varphi' + br(\varphi')\sin\varphi'}{c} \tag{8}$$

2.2. Parametric equation of the line of intersection on the unfolded cylinder

We will find a transformation for eqn (8). Fig. 1(b) shows the top view of the unfolded cylinder. The original cylinder is shown by a dashed line. The cylinder is unrolled in the clockwise direction while keeping its intersection with the XZ plane in the +X direction stationary. How any point P on the cylinder moves and relocates as P′ is shown by a brown curved arrow.

The transformation is denoted by:

$$x \to \tilde{x}$$
$$y \to \tilde{y}$$
$$z \to \tilde{z}$$

From Fig. 1(b)

$$\tilde{x} = r \tag{9}$$

$$\tilde{y} = \int_0^{\varphi'} r(\varphi')d\varphi' \tag{10}$$

$$\tilde{z} = z \tag{11}$$

The parametric equation of the line after unrolling the image is defined by equations (8) and (10).

Putting $\alpha = \beta = r$ in eqn (6) we get $r(\varphi') = r$, which is the equation of a cylinder with a circular cross-section with radius r. Without loss of generality take $r = 1$ unit and scale all other measurements accordingly. In such a case, the parametric equations of the line simplifies to

$$y(\varphi') = \varphi' \tag{12}$$

$$z(\varphi') = -\frac{a\cos\varphi' + b\sin\varphi}{c} \tag{13}$$

We will use this circular cross-sectional cylinder for all the subsequent derivations as that is the case with drill cores. The tilde symbol above y and z has been dropped in eqns (12) and (13), respectively, because we will use these as more general equations, and present all the derivations in the YZ plane itself. One can look at this as another Cartesian system with its origin at (1,0,0) of the coordinate system associated with the cylinder in Fig. 1(a).

2.3. Geological relevance

For eqn (13) to make more geological sense, a, b and c need to be defined in terms of dip (θ) and dip direction (φ) of the plane. Consider the +X direction to be north and consequently + Y to be west.

Consider the plane, and points P and Q shown in Fig. 2(a). P is at unit distance from the origin, along the line of maximum dip. In other words, the line has a rake or pitch of 90°. Q is the unit distance from origin on the XY plane (i.e. along the strike of the plane).

Let $P = (x_1, y_1, z_1)$ and. $Q = (x_2, y_2, 0)$

Resolving the OP length into components along the Z-axis and the

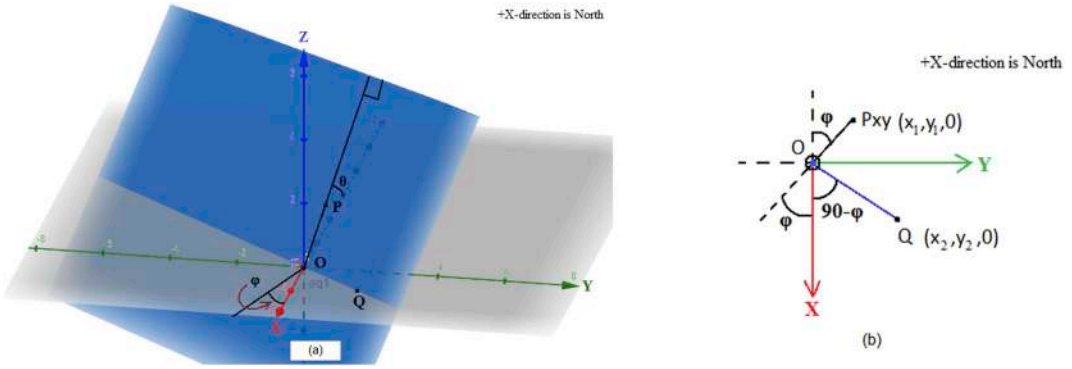

Fig. 2. (a): A blue plane passing through the origin (O) that dips θ towards φ. View subsection 2.3 for meaning of other symbols. **(b):** Plan view of the previous subfigure. See Section 2.3 for details. (For interpretation of the references to colour in this figure legend, the reader is referred to the Web version of this article.)

XY-plane:

$$z_1 = \sin\theta \tag{14}$$

Now consider the top view of Fig. 2(a) shown in Fig. 2(b). Here P_{xy} is the projection of P on the XY plane. Therefore, $OP_{xy} = \cos\theta$ units and $OQ = 1$ unit. The following relations are obtained

$$x_1 = -OP_{xy}\cos\varphi = -\cos\theta\cos\varphi \tag{15}$$

$$y_1 = OP_{xy}\sin\varphi = \cos\theta\sin\varphi \tag{16}$$

$$x_2 = OQ\sin\varphi = \sin\varphi \tag{17}$$

$$y_2 = OQ\cos\varphi = \cos\varphi \tag{18}$$

Putting $x = x_2$, $y = y_2$ from equations (17) and (18), respectively, and $z = 0$ in eqn (7)

$$a\sin\varphi + b\cos\varphi = 0 \tag{19}$$

$$\therefore b = -a\tan\varphi \tag{20}$$

Putting $x = x_1$, $y = y_1$ and $z = z_1$ from eqns (14)–(16) in eqn (7) and substituting b from eqn (20)

$$-a\cos\theta\cos\varphi - a\tan\varphi\cos\theta\sin\varphi + c\sin\theta = 0 \tag{21}$$

$$\Rightarrow c\sin\theta = a\left(\cos\varphi + \frac{\sin^2\varphi}{\cos\varphi}\right)\cos\theta \tag{22}$$

$$\Rightarrow c\sin\theta = a\left(\frac{\cos^2\varphi + \sin^2\varphi}{\cos\varphi}\right)\cos\theta \tag{23}$$

$$\therefore c = a\frac{\cot\theta}{\cos\varphi} \tag{24}$$

Substituting the relations from eqn (20) and eqn (24) back into eqn (7):

$$ax - \frac{a\sin\varphi}{\cos\varphi}y + \frac{a\cot\theta}{\cos\varphi}z = 0 \tag{25}$$

$$\Rightarrow (\cos\varphi)x - (\sin\varphi)y + (\cot\theta)z = 0 \tag{26}$$

Comparing eqn (26) with eqn (7), we can write:

$$a = \cos\varphi \tag{27}$$

$$b = -\sin\varphi \tag{28}$$

$$c = \cot\theta \tag{29}$$

Therefore, eqn (13) is re-written:

$$z = -\frac{\cos\varphi\cos\varphi' - \sin\varphi\sin\varphi'}{\cot\theta} \tag{30}$$

$$\Rightarrow z = -\cos(\varphi + \varphi')\tan\theta \tag{31}$$

This is the equation of a sinusoid with a wavelength 2π, with an amplitude of $\tan\theta$ and a phase of φ. Mattioni et al. (2010) in the caption of their Fig. 3 refer the dip of the plane as to equal $\tan^{-1}\left(\frac{h}{2\rho}\right)$ where h is the height of the sinusoid that can be obtained from the unrolled image, and ρ is the radius of the drill core.

If the plane does not pass through the origin, an additional variable d is added in eqn (30)

$$z = -(\cos\varphi\cos\varphi' - \sin\varphi\sin\varphi' + d)\tan\theta \tag{32}$$

Using the MATLAB programming (Appendix A), in Fig. 3(a)–(h) the above relation has been plotted with Y as the horizontal Cartesian axis and Z along the vertical axis for the cylinder with a circular cross-section in blue. The lines in red show the corresponding plots for the cylinder with an elliptical cross-section as shown in Fig. 1(a) for a more generalized derivation. Fig. 3(a)–(h) show the plots for the same dip amount and different dip direction of the plane. Fig. 3(i) presents how planes of different dip but with the same dip direction would ideally appear in an unrolled image. Logically, it can be stated that a horizontal and a vertical plane will plot as horizontal and vertical lines, respectively in unrolled images.

2.4. Equations of the line in unrolled image for an inclined core

In case the cylindrical core is inclined, as can be the case in geo-steering problems, we would essentially be dealing with two co-ordinate systems, the co-ordinate system defined so far (X, Y, Z) and the co-ordinate system of the cylinder denoted by (X_c, Y_c, Z_c) (Fig. 4), tilted with respect to each other by some angle.

Consider the simple case where the cylinder plunges at an angle λ and trends 0°. Note $\gamma = (90° - \lambda)$. This rotation takes the old co-ordinate system (left hand side column in matrices in eqns (33) and (34)) into the new co-ordinate system (right hand side column in those eqns). The coordinate transformation can be represented by the matrix equation (as per Arfken George et al., 2007):

$$\begin{bmatrix} x \\ y \\ z \end{bmatrix} = \begin{bmatrix} \cos\gamma & 0 & -\sin\gamma \\ 0 & 1 & 0 \\ \sin\gamma & 0 & \cos\gamma \end{bmatrix}\begin{bmatrix} x_c \\ y_c \\ z_c \end{bmatrix} \tag{33}$$

$$\begin{bmatrix} x \\ y \\ z \end{bmatrix} = \begin{bmatrix} \sin\lambda & 0 & -\cos\lambda \\ 0 & 1 & 0 \\ \cos\lambda & 0 & \sin\lambda \end{bmatrix}\begin{bmatrix} x_c \\ y_c \\ z_c \end{bmatrix} \tag{34}$$

Therefore, combining eqns (26) and (34):

$$\cos\varphi[(\sin\lambda)x_c - (\cos\lambda)z_c] - (\sin\varphi)y_c + \cot\theta[(\cos\lambda)x_c + (\sin\lambda)z_c] = 0 \tag{35}$$

$$(\cos\varphi\sin\lambda + \cot\theta\cos\lambda)x_c - (\sin\varphi)y_c - (\cos\varphi\cos\lambda - \cot\theta\sin\lambda)z_c = 0 \tag{36}$$

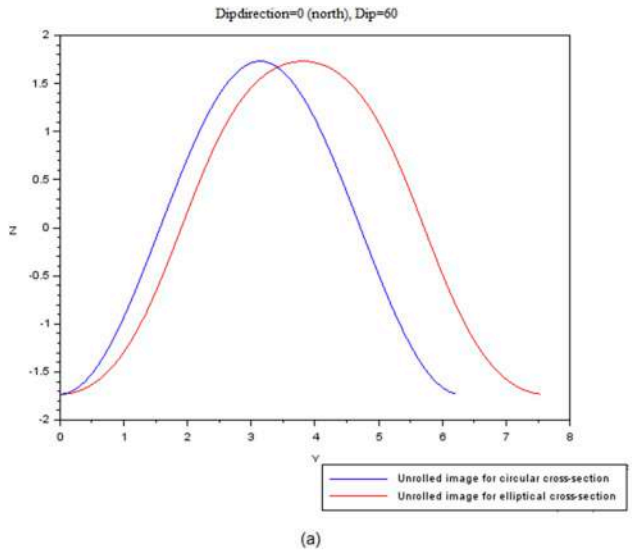

(a)

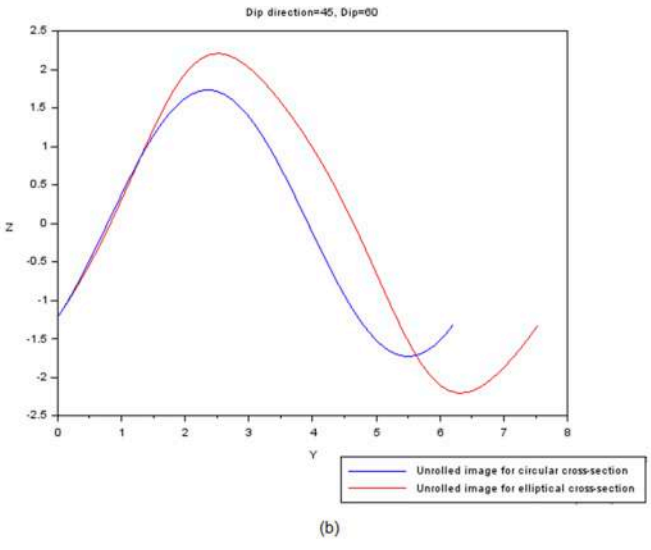

(b)

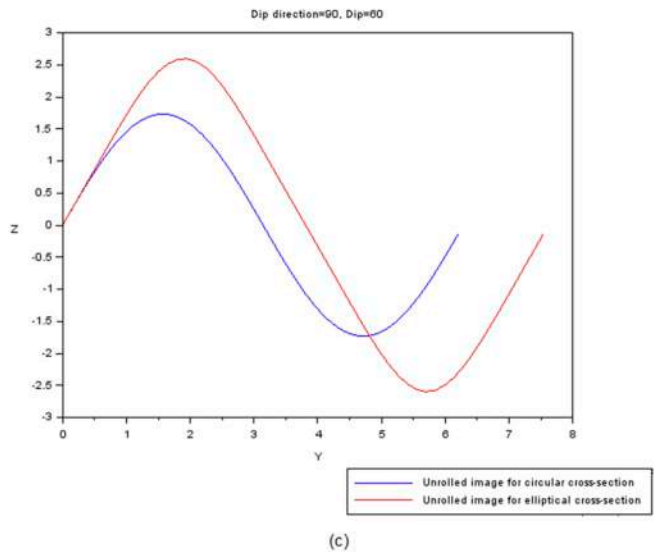

(c)

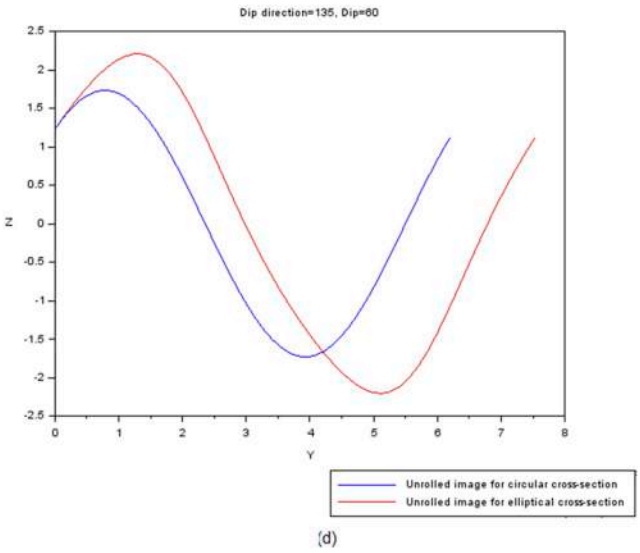

(d)

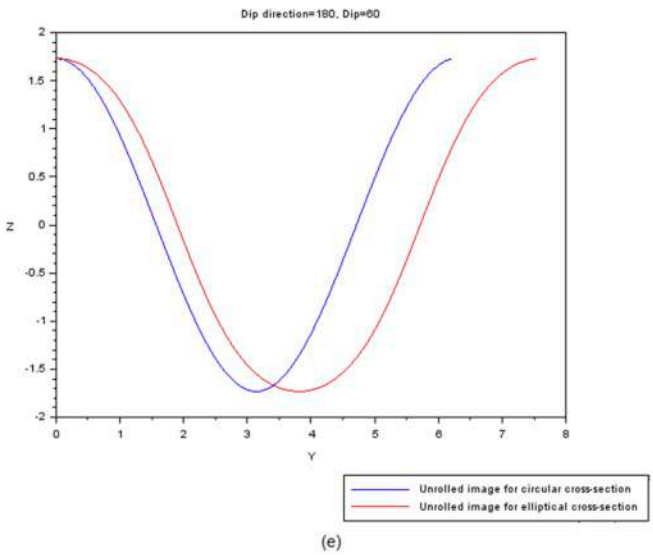

(e)

Fig. 3. (a–h) Ideal unrolled images showing planes for different dip directions but same dip amount. Blue lines indicate the situation for the circular cross-section. Red lines connote the case for elliptical cross section. **(i):** Ideal unrolled images showing planes for different dip amounts but same dip direction. See Section 2.3 for details. (For interpretation of the references to colour in this figure legend, the reader is referred to the Web version of this article.)

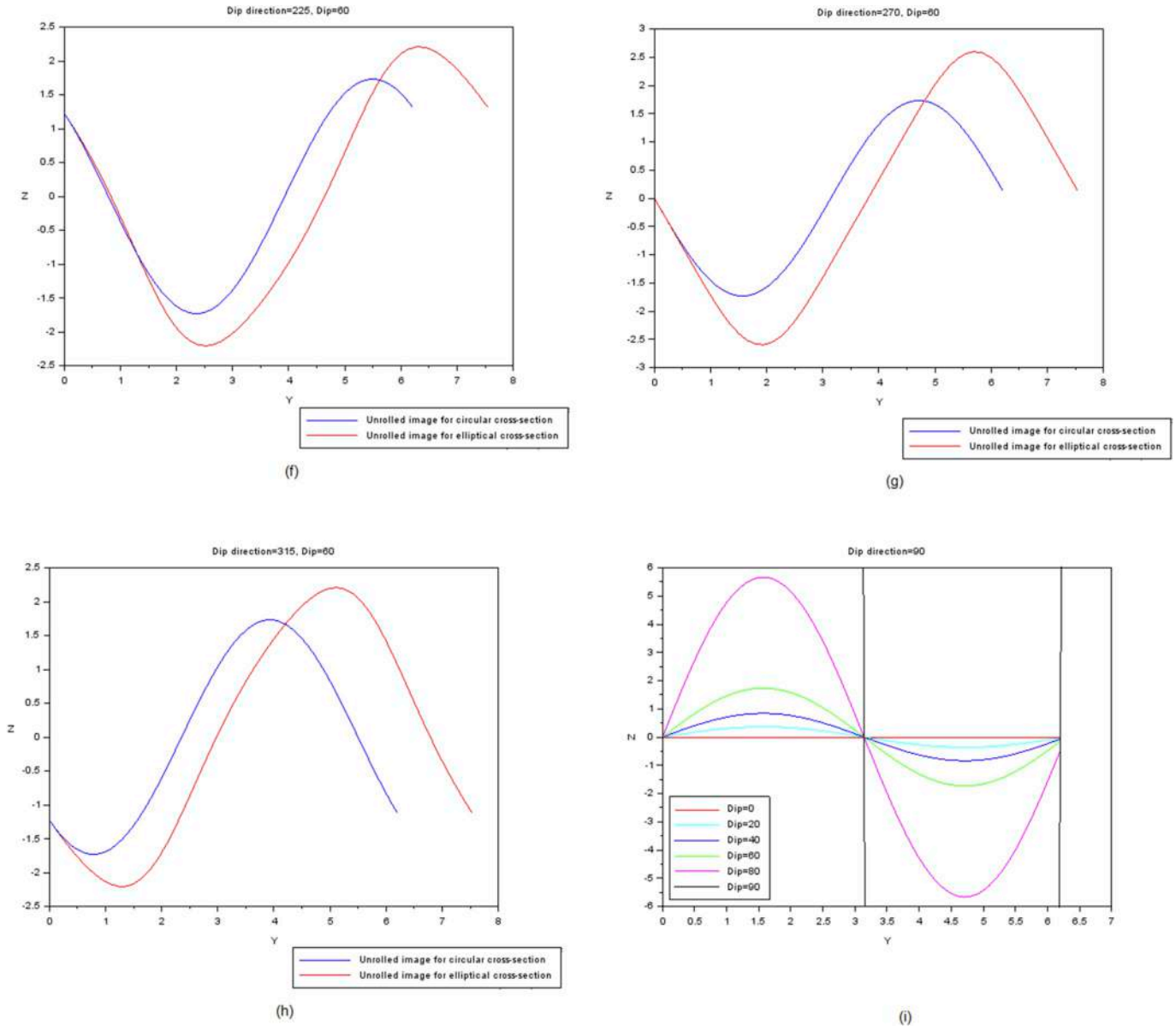

Fig. 3. (*continued*)

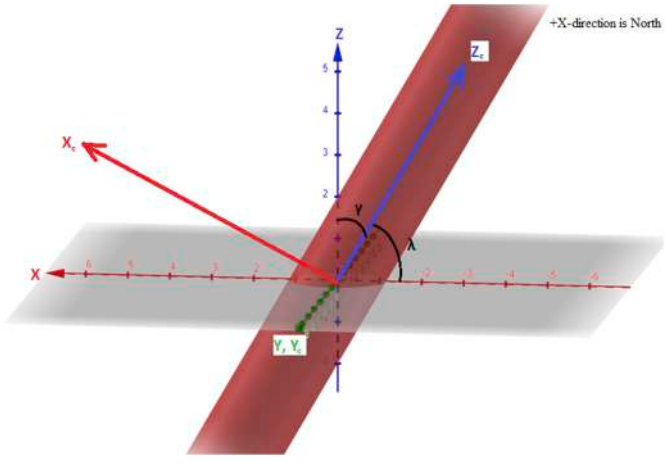

Fig. 4. Coordinate system (X_c, Y_c, Z_c) associated with an inclined core plunging towards North (i.e., the X-axis of the co-ordinate system as used in previous figures). λ: plunge of the drill core; $\gamma = (90^\circ - \lambda)$. See Section 2.4 for details.

Fig. 5(a) shows a plane with dip direction = 270° and dip = 60° and a core plunging 45° towards north. Using the MATLAB programming as done in Appendix 2, Fig. 5(b) shows the corresponding unrolled image. One can compare this with Fig. 3(g) and notice the difference in phases and amplitudes.

Now consider a more general case where, the core trends Φ (Fig. 6). This would involve a rotation of Φ about the Z-axis, followed by a rotation of γ about the Y axis. Therefore, the corresponding equation for the transformation becomes,

$$\begin{bmatrix} x \\ y \\ z \end{bmatrix} = \begin{bmatrix} \cos\Phi & \sin\Phi & 0 \\ -\sin\Phi & \cos\Phi & 0 \\ 0 & 0 & 1 \end{bmatrix} \begin{bmatrix} \sin\lambda & 0 & -\cos\lambda \\ 0 & 1 & 0 \\ \cos\lambda & 0 & \sin\lambda \end{bmatrix} \begin{bmatrix} x_c \\ y_c \\ z_c \end{bmatrix} \tag{37}$$

$$\begin{bmatrix} x \\ y \\ z \end{bmatrix} = \begin{bmatrix} \cos\Phi\sin\lambda & \sin\Phi & -\cos\Phi\cos\lambda \\ -\sin\Phi\sin\lambda & \cos\Phi & \sin\Phi\cos\lambda \\ \cos\lambda & 0 & \sin\lambda \end{bmatrix} \begin{bmatrix} x_c \\ y_c \\ z_c \end{bmatrix} \tag{38}$$

Combining eqns (26) and (38):

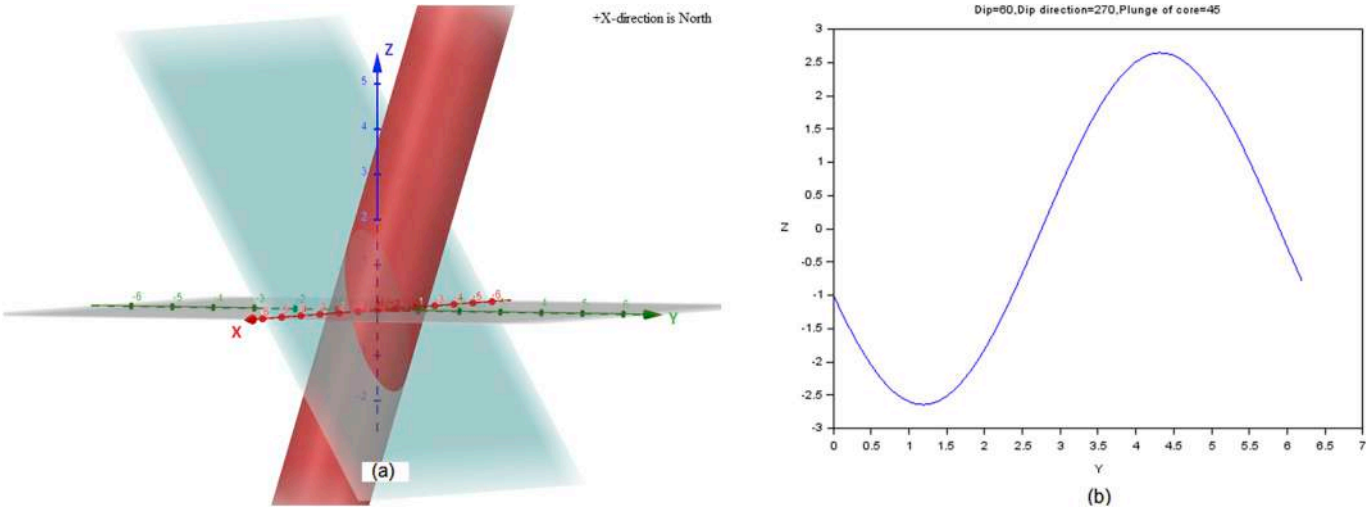

Fig. 5. (a): A north trending inclined drill core is cut by an inclined plane. **(b):** Unrolled image of the inclined plane of the previous subfigure. See Section 2.4 for details.

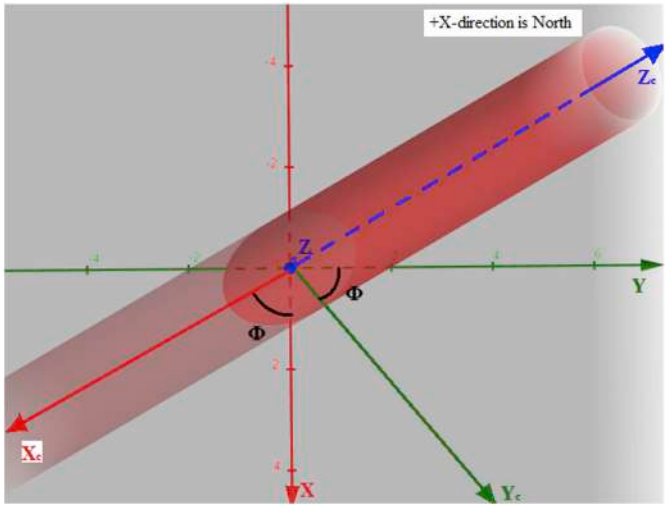

Fig. 6. Coordinate system (X_c, Y_c, Z_c) associated with an inclined core plunging towards Φ. See Section 2.4 for details.

$$\cos\varphi[(\cos\Phi\sin\lambda)x_c + (\sin\Phi)y_c - (\cos\Phi\cos\lambda)z_c] + \sin\varphi [(\sin\Phi\sin\lambda)x_c - (\cos\Phi)y_c - (\sin\Phi\cos\lambda)z_c] + \cot\theta[(\cos\lambda)x_c + (\sin\lambda)z_c] = 0 \quad (39)$$

$$\frac{(\cos\varphi\cos\Phi\sin\lambda + \sin\varphi\sin\Phi\sin\lambda + \cot\theta\cos\lambda)}{(\cos\varphi\cos\Phi\cos\lambda + \sin\varphi\sin\Phi\cos\lambda - \cot\theta\sin\lambda)}x_c + \frac{(\cos\varphi\sin\Phi - \sin\varphi\cos\Phi)}{(\cos\varphi\cos\Phi\cos\lambda + \sin\varphi\sin\Phi\cos\lambda - \cot\theta\sin\lambda)}y_c = z_c \quad (40)$$

Fig. 7(a) shows a plane with dip direction = 270° and dip = 60° and a core that plunges 45° and trends 60°. Using the MATLAB programming as done in Appendix 2, Fig. 7(b) shows the corresponding appearance of the plane in an unrolled image. One can compare this with Fig. 5(b) and see the difference. Note that bedding plane orientations and their dips are studied through image logs (e.g., Zhang et al., 2014).

2.5. Observations for different geological features

2.5.1. A pair of fractures

Orthogonal fractures These fractures intersect at right angle to each other (e.g., Fig. 7.6 in van der Pluijm and Marshak, 2004). With

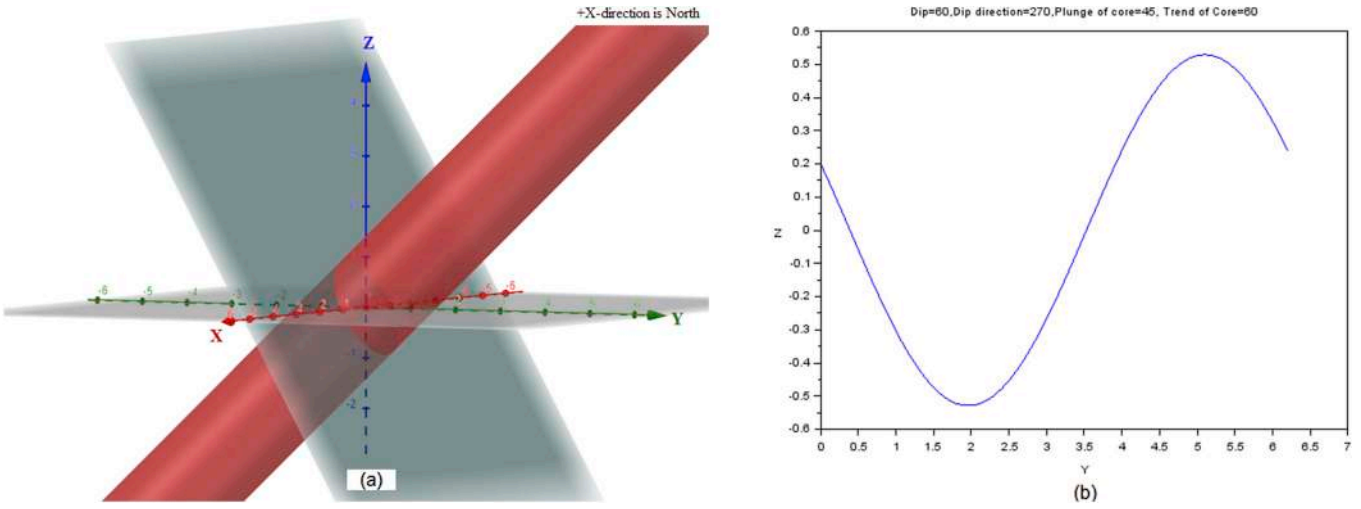

Fig. 7. (a): An inclined core plunging in a direction other than North. The core is cut by an inclined plane. **(b):** Unrolled image showing the inclined plane of the previous subfigure. See Section 2.4 for details.

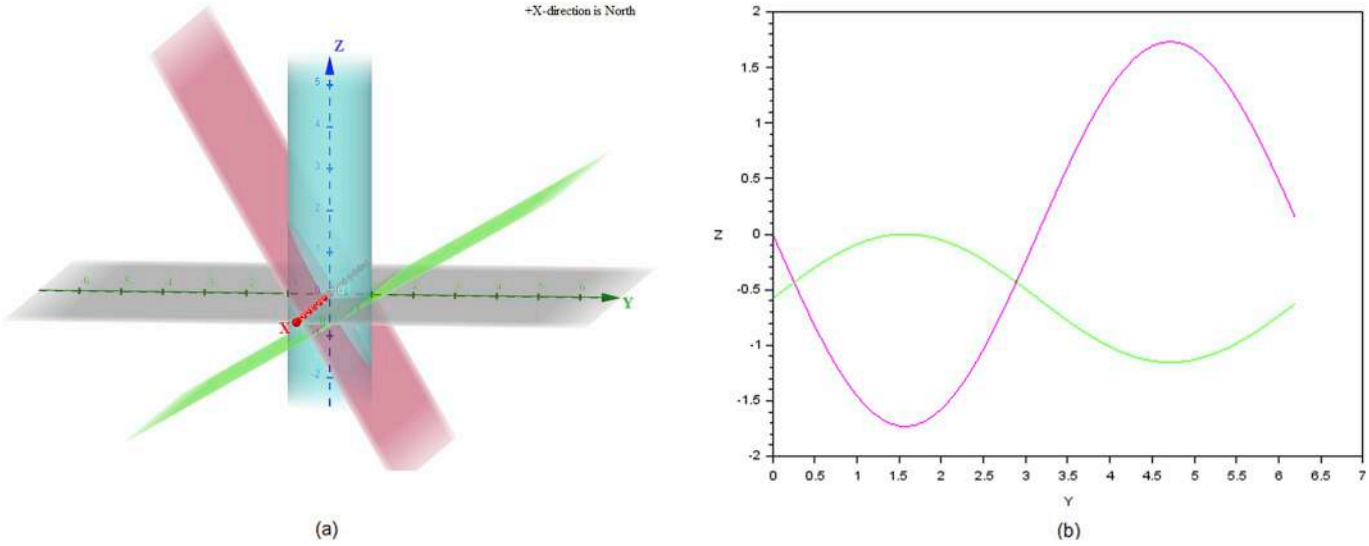

Fig. 8. (a): Orthogonal fractures intersect a vertical drill core. **(b):** Unrolled image showing the orthogonal fractures of the previous subfigure. See Section 2.5.1.1 for details.

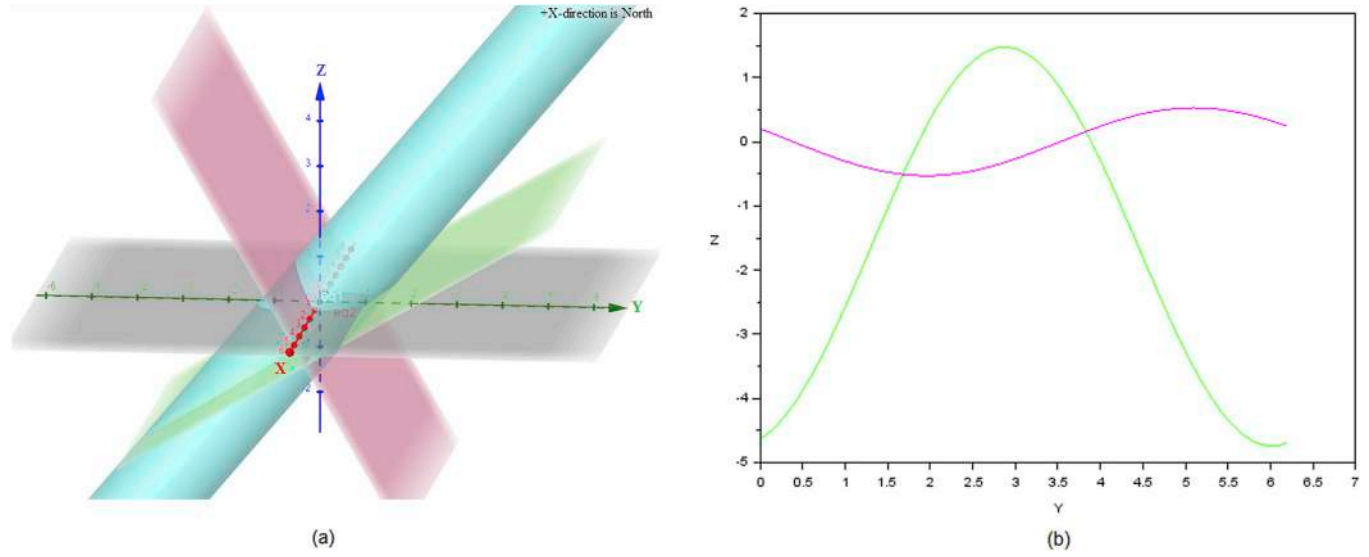

Fig. 9. (a): Orthogonal fractures intersect an inclined drill core. **(b):** Unrolled image showing the orthogonal fractures of the previous subfigure. See Section 2.5.1.1 for details.

reference to eqn (32), we choose the following two planes:

(i) $\varphi = 270°; \theta = 60°; d = 0$ (ii) $\varphi = 90°; \theta = 30°; d = 1$

Fig. 8(a) shows these two planes and a vertical drill core. Using the MATLAB programming as done in Appendix 1, Fig. 8(b) shows the corresponding graph.

Fig. 9(a) shows these two planes and an inclined drill core plunging 45° and trending 60°. Using the MATLAB programming as done in Appendix 2, Fig. 9(b) shows the corresponding graph, which shows that the two curves representing the two planes. have quite dissimilar geometries. Conjugate fractures With reference to eqn (32), we choose the following two planes that intersect at 60°. This is the most common angular relation in natural conjugate fractures (McHone et al., 2005).

(i) $\varphi = 270°; \theta = 60°; d = 0$ (ii) $\varphi = 90°; \theta = 60°; d = 1$

Fig. 10(a) shows these two planes and a vertical drill core. Using the MATLAB programming as done in Appendix 1, Fig. 10(b) shows the corresponding graph.

Fig. 11(a) shows conjugate fractures cut by an inclined drill core plunging 45° and trending 60°. Using the MATLAB programming as done in Appendix 2, Fig. 11(b) shows the corresponding graph.

2.5.2. Folds

Single generation foldsWe use a simple cosine equation (e.g., Bastida et al., 2005, and references therein) to represent a periodic fold (similar to Ghosh, 1993).

$$z = a\cos b(y - c) \tag{41}$$

The curve extends along the X-axis along both the sides. In other words, it is a single generation periodic fold where the fold axis parallels the X-axis. Here, a is the amplitude, b is related to its wavelength (λ) as $\lambda = \frac{2\pi}{b}$ and c is its phase (Fig. 12). Fig. 12 utilizes the MATLAB programming as shown in Appendix 3.

Consider a vertical cylinder of unit radius for its circular cross-section. For simplicity take a = 1 in eqn (41). Combining eqns (1), (2), (12) and (41) the parametric equation of the line of intersection on the

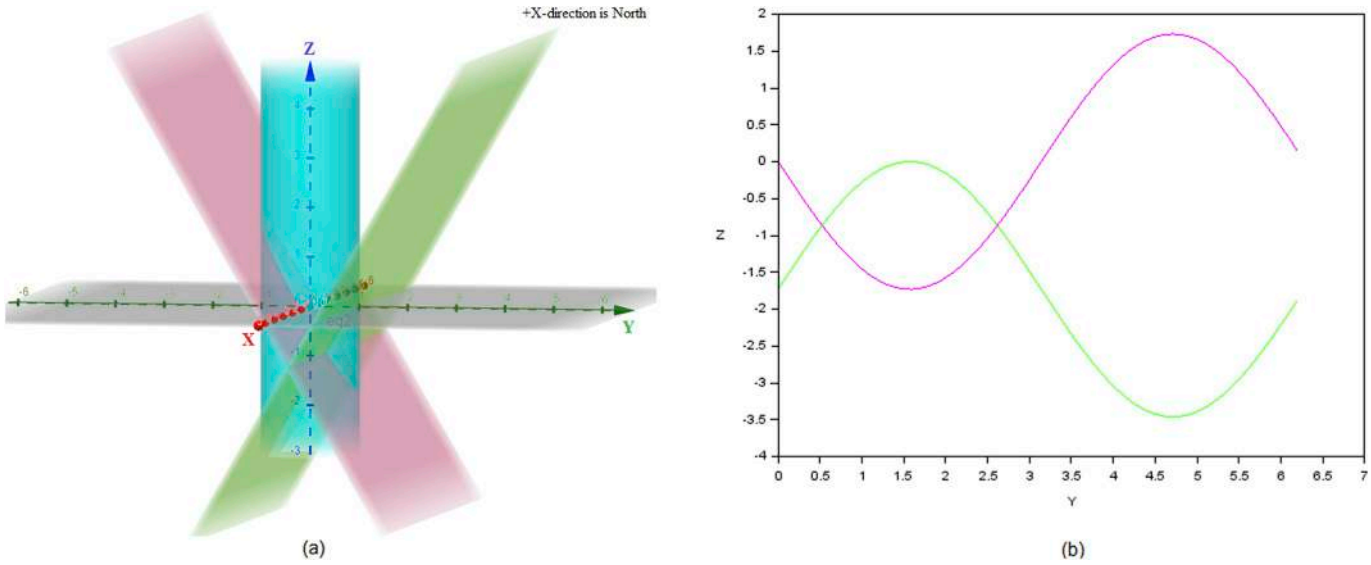

Fig. 10. (a): Conjugate fractures meeting at 60° intersect a vertical drill core. **(b):** Unrolled image showing the conjugate fractures of the previous subfigure. See Section 2.5.1.2 for details.

unfolded cylinder, becomes:

$$y(\varphi') = \varphi' \tag{42}$$

$$z(\varphi') = \cos b(\sin\varphi' - c) \tag{43}$$

Fig. 13(a) shows three folds with different magnitudes of b. How the unrolled images of such folds look like is presented in Fig. 13(b), which utilizes the MATLAB programming shown in Appendix 4. Fig. 14(a) shows the folds for different values of c. How the unrolled images of such folds look like is presented in Fig. 14(b), which comes from the MATLAB programming shown in Appendix 4.

We will generate ideal unrolled images for the fold cases, as in Figs. 12a and 13a, for the inclined drill core situation as per Section 2.4. Combining eqns (38) and (41):

$$(\cos\lambda)x_c + (\sin\lambda)z_c = a\cos b[-(\sin\Phi\sin\lambda)x_c + (\cos\Phi)y_c + (\sin\Phi\cos\lambda)z_c - c] \tag{44}$$

Substituting x_c by $\cos\varphi'$ and y_c by $\sin\varphi'$ in eqn (44):

$$\cos\lambda\cos\varphi' + (\sin\lambda)z_c = a\cos b[-(\sin\Phi\sin\lambda\cos\varphi' + \cos\Phi\sin\varphi' + (\sin\Phi\cos\lambda)z_c - c] \tag{45}$$

Equations such as 44 and 45 cannot be solved analytically but can be determined numerically. Superposed folds A type-1 fold is a specific case of refolding of a pre-existing fold, with fold axes parallel to the X-axis and the Y-axis respectively. Let the eqn of the first generation fold be

$$z = a_y\cos b_y(y - c_y) \tag{46}$$

Here, a_y, b_y and $c_y$are equivalent to the symbols *a*, *b* and *c* of Fig. 12. Let the eqn of the second generation fold be

$$z = a_x\cos b_x(x - c_x) \tag{47}$$

Here, a_x, b_x and $c_x$are equivalent to the symbols *a*, *b* and *c* of Fig. 12. Therefore, the equation of the superposed fold is given by:

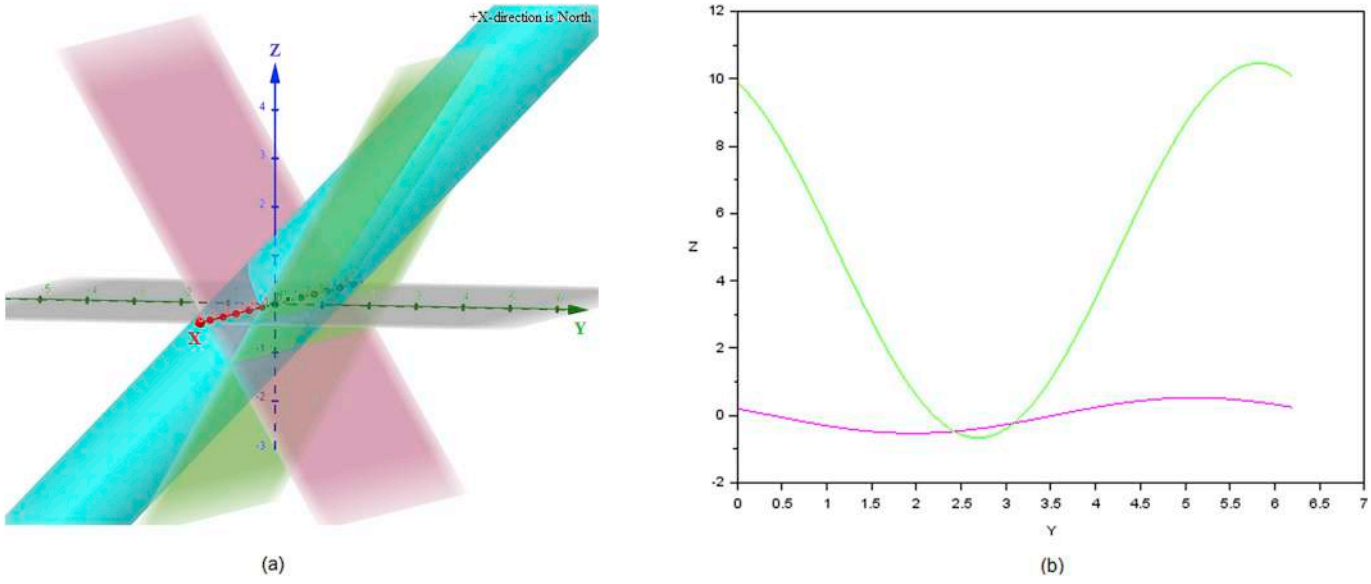

Fig. 11. (a): Conjugate fractures meeting at 60° intersect an inclined drill core. **(b):** Unrolled image showing the conjugate fractures of the previous subfigure. See Section 2.5.1.2 for details.

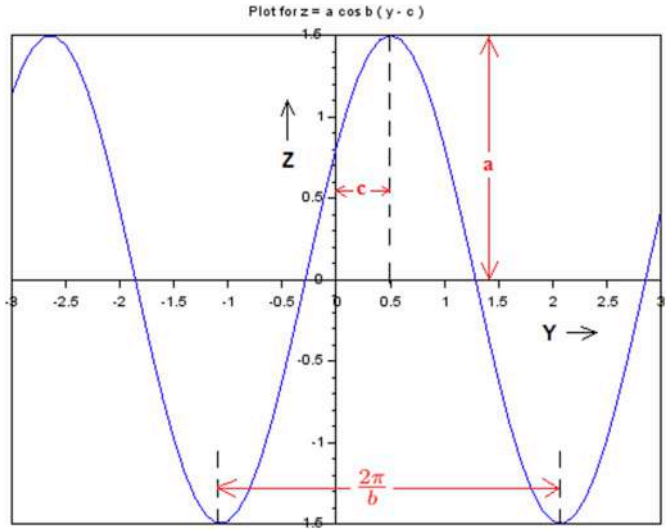

Fig. 12. A fold profile is shown. Subsection 2.5.2. defines symbols See Section 2.5.2.1 for details.

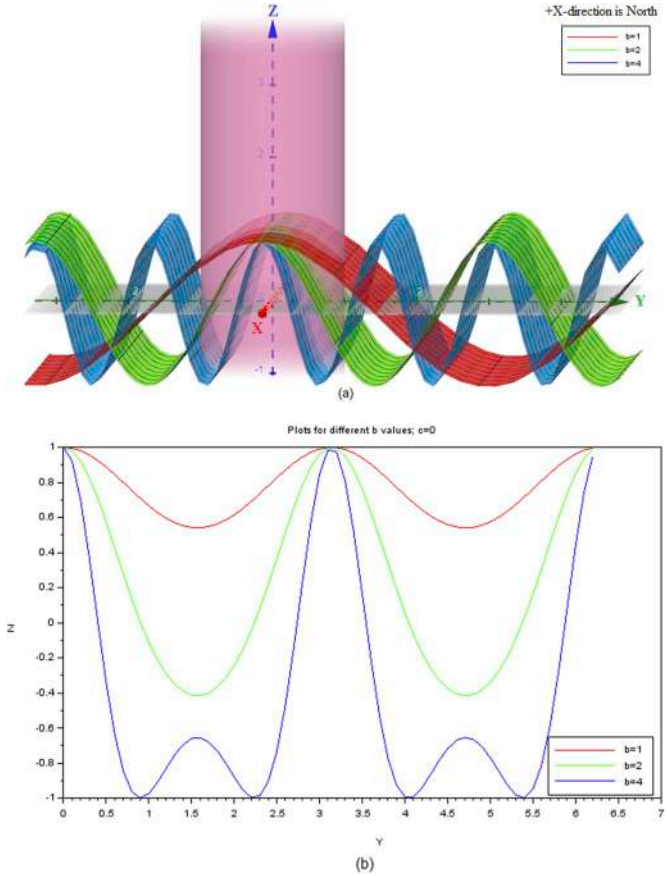

Fig. 13. (a): Folds with different b values. For details about see subsection 2.5.2. **(b):** Unrolled images showing the folds in the previous subfigure. See Section 2.5.2.1 for details.

$$z = a_y \cos b_y (y - c_y) + a_x \cos b_x (x - c_x) \tag{48}$$

Combining eqns (1), (2) and (48), the equation of the line of intersection between the fold and the core in the unrolled image becomes:

$$z(\varphi') = a_y \cos b_y (\sin\varphi' - c_y) + a_x \cos b_x (\cos\varphi' - c_x) \tag{49}$$

Fig. 15(a) and (a′) show the same type-1 fold observed from different angles of views with the parameters $a_x = a_y = 1$, $c_x = c_y = 0$,

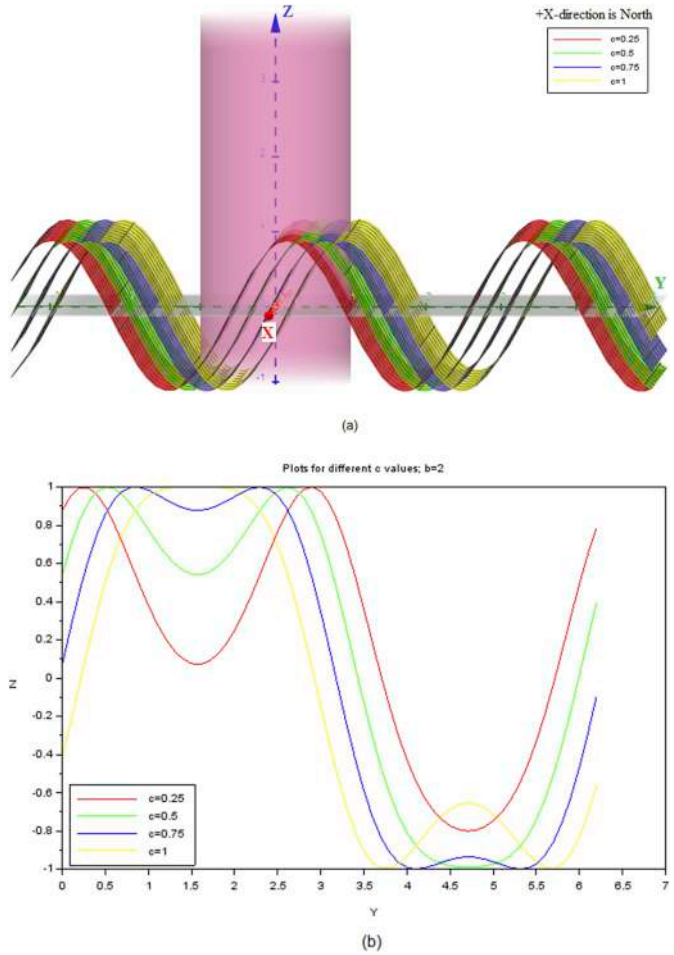

Fig. 14. (a): Folds with different c values. For details about see subsection 2.5.2. **(b):** Unrolled images showing the folds in the previous subfigure. See Section 2.5.2.1 for details.

$b_x = 0.5$ and $b_y = 3$. Fig. 15(b) shows the corresponding unrolled image. This figure utilizes the MATLAB programming shown in Appendix 5. The curve in Fig. 15(b) is noticably different from that of a dipping plane such as in Fig. 5(b). A type-2 fold can be seen as a superposed fold with axis of the second generation fold parallel to the Z-axis. Because of the second generation folding, the axis of the first generation fold, which was initially parallel to the X-axis, gets folded. Let the eqn of the first generation fold be

$$z = a_y \cos b_y (y - c_y) \tag{50}$$

Here, a_y, b_y and $c_y$are equivalent to the symbols *a*, *b* and *c* of Fig. 12. Let the eqn of the second generation fold be

$$y = a_x \cos b_x (x - c_x) \tag{51}$$

Here, a_x, b_x and $c_x$are equivalent to the symbols *a*, *b* and *c* of Fig. 12. Therefore, the equation of the superposed fold is given by:

$$z = a_y \cos b_y [y - c_y - a_x \cos b_x (x - c_x)] \tag{52}$$

Combining equations (1), (2) and (52), the equation of the line of intersection between the fold and the core in the unrolled image becomes:

$$z(\varphi') = a_y \cos b_y [\sin\varphi' - c_y - a_x \cos b_x (\cos\varphi' - c_x)] \tag{53}$$

Fig. 16(a-c) shows a type-2 fold with the specific vertical drill locations. In Fig. 16(a) $a_x = -1$, $a_y = 1$, $c_x = 0$, $c_y = 1$, $b_x = 1$ and $b_y = 2$. In Fig. 16(b) $a_x = -1$, $a_y = 1$, $c_x = 1$, $c_y = 0.5$, $b_x = 1$ and $b_y = 2$. In Fig. 16(c) $a_x = -1$, $a_y = 1$, $c_x = 2$, $c_y = -0.5$, $b_x = 1$ and $b_y = 2$.

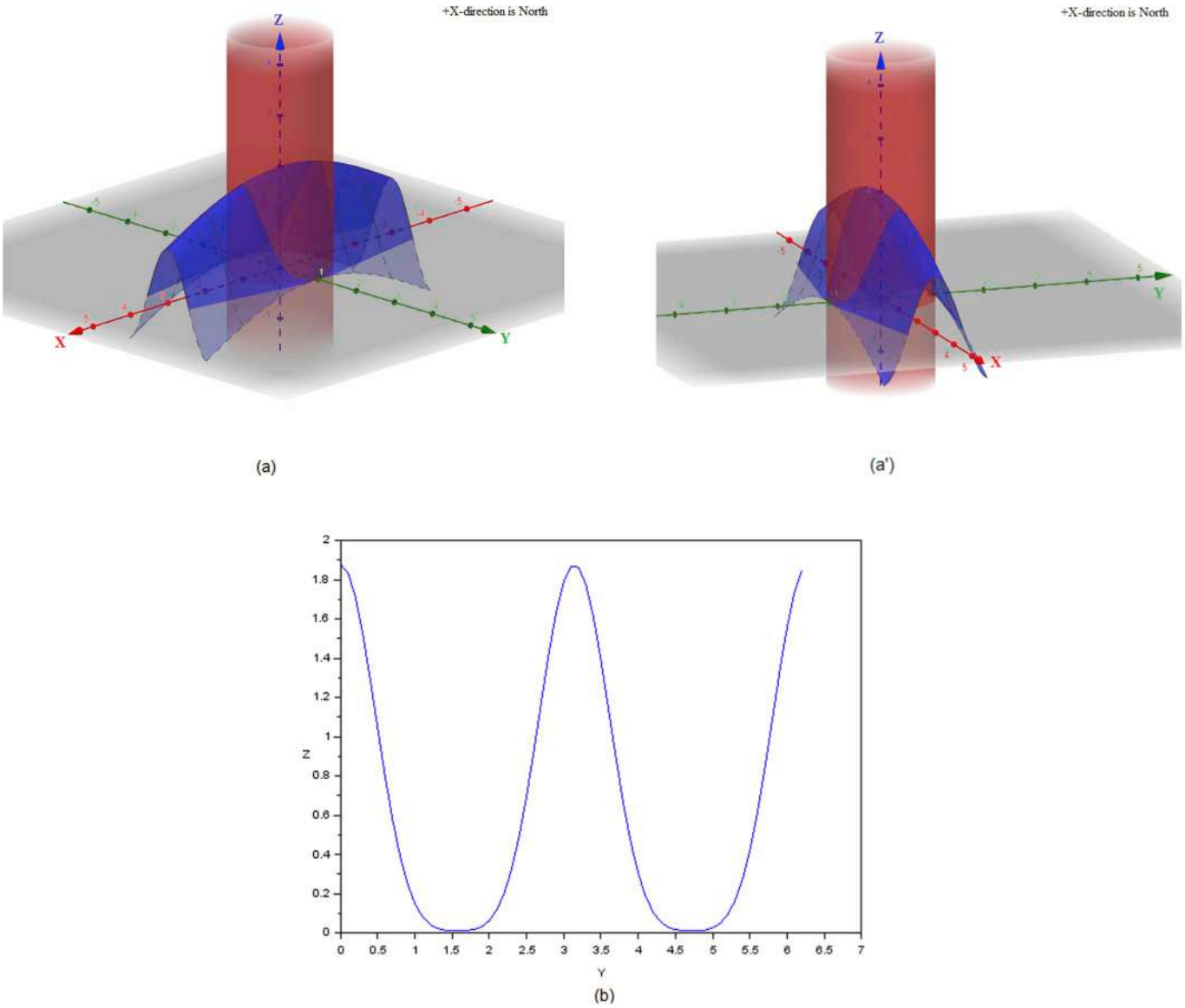

Fig. 15. (a): A vertical drill core intersects a type-1 superposed fold at its hinge zone. **(a′):** The previous subfigure is shown from a different angle. **(b):** Unrolled image of the fold as shown in the previous subfigure. See Section 2.5.2.2 for details.

Fig. 16(a′-c′), that have been generated using the MATLAB programming as shown in Appendix 6, show the corresponding unrolled images. Depending on the drill locations, one can note changes in the manifestations of the fold in the unrolled images. Also, one can track the curves in the unrolled images along the X-axis to note changes in their geometries. This obviously does not happen for a uniformly dipping plane as observed in its unrolled image (such as Fig. 5(b)).

Type 3 folds can be seen as a superposition of two folds, both with fold axes parallel to the X-axis, and compression in horizontal and vertical directions, respectively. The equations of these two folds can be written as:

$$z = a_y \cos b_y (y - c_y) \tag{54}$$

$$y = a_z \cos b_z (z - c_z) \tag{55}$$

These are recursive equations in y and z and hence, difficult to solve analytically.

2.5.3. Listric faults

General points Though reported by Marshak and Mitra (1988), actual quantification of 3D or even the 2D equation of listric faults does not exist. Madariaga (1976) considers circular-shaped listric faults. Benjemaa et al. (2007) opt for parabolic listric fault plane in their numerical model. Oakley (2017) models deformation for both circular and non-circular listric faults. Schultz (1987, 1992) in his numerical models took listric strike-slip faults as circular arcs. Mukherjee and Tayade (2019) and Mukherjee and Chakraborty (2020) recently perform numerical model on the kinematics of rotational listric faulting on spherical fault surfaces. Parabolic/paraboloidal slip surface is inferred from the Mohr-Coulomb failure criteria (e.g., Wriggers et al., 1990). Ritz (2013) fits sinusoidal curves with listric faults. Cylindrical fault geometries are used in the models by Ellis and McClay (1988) and Lohr et al. (2008). Yamada and McClay (2003) use irregular listric geometry of listric faults in their models.

In the subsequent sub-section we will deal with listric faults of ideal geometries and deduce their appearances in unrolled images. Spherical surface Consider the fault surface to be a portion of a spherical surface:

$$(x - h)^2 + (y - k)^2 + z^2 = R^2 \tag{56}$$

The sphere has a centre at $(h, k, 0)$, lying on the XY-plane, with a

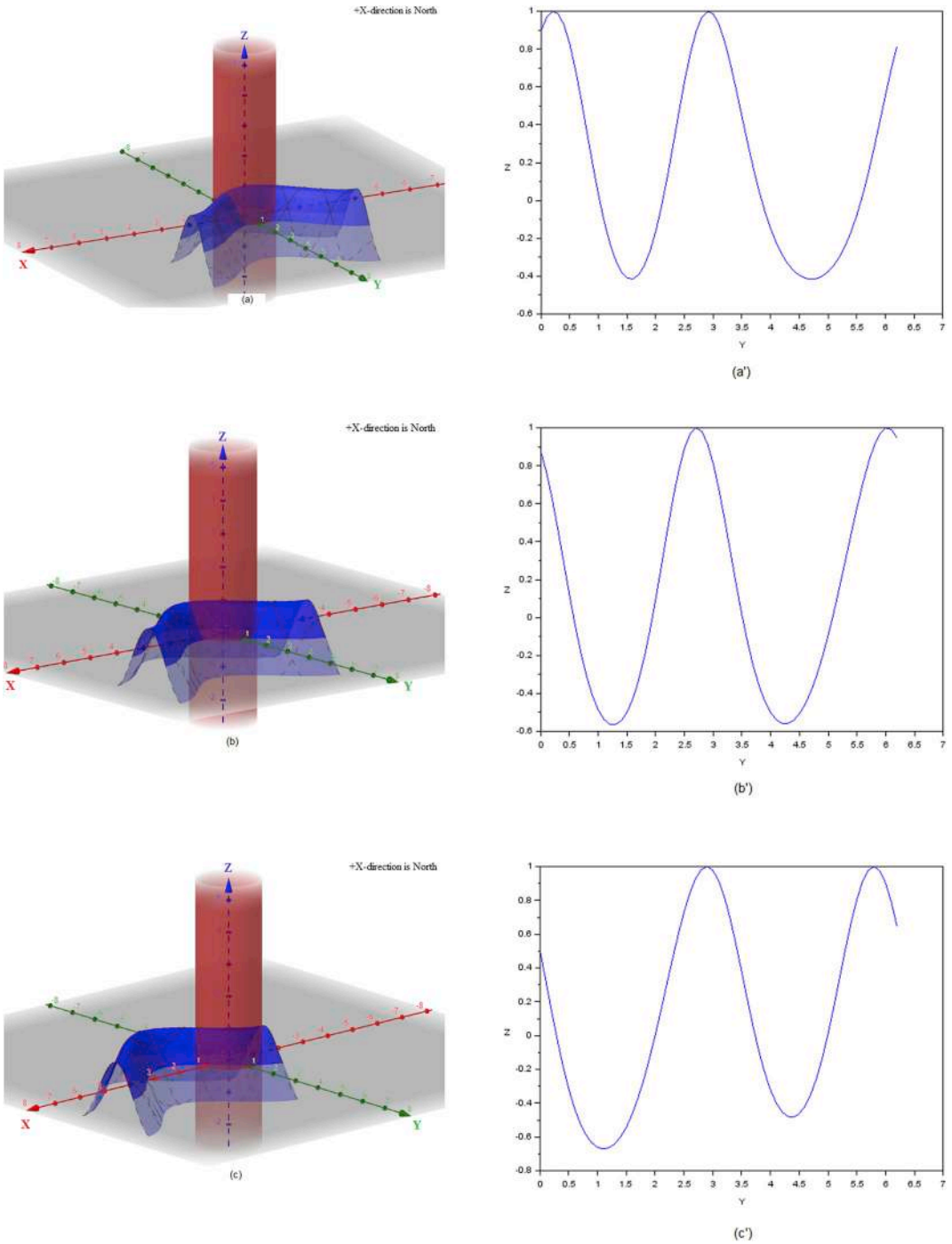

Fig. 16. (a): A vertical drill core intersects a type-2 superposed fold at its hinge zone. **(a′):** Unrolled image of the fold as shown in the previous subfigure. **(b):** A vertical drill core intersects a type-2 superposed fold. Drilling is done at a position different from the previous case. **(b′):** Unrolled image of the fold as shown in the previous subfigure. **(c):** A vertical drill core intersects a type-2 superposed fold. Drilling is done at a position different from the previous two cases. **(c′):** Unrolled image of the fold as shown in the previous subfigure. See Section 2.5.2.2 for details.

radius R.

The equation of the line of intersection between the cylinder and the spherical listric fault plane is, from eqns (1), (2) and (56) is:

$$z(\varphi') = \sqrt{R^2 - (\cos\varphi' - h)^2 - (\sin\varphi' - k)^2} \tag{57}$$

Fig. 17(a) shows a part of a sphere with $h = 2$, $k = 3$ and $R = 5$, and the cylinder with unit circular cross-section. Fig. 17(b) is the corresponding unrolled image, that utilizes the MATLAB programming as shown in Appendix 7: Paraboloidal surface. Consider the fault surface to be the paraboloid:

$$(x - h)^2 + (y - k)^2 = az \tag{58}$$

with the centre at $(h, k, 0)$. The equation of the line of intersection between this listric fault plane and the drill core, from eqns (1), (2) and (58):

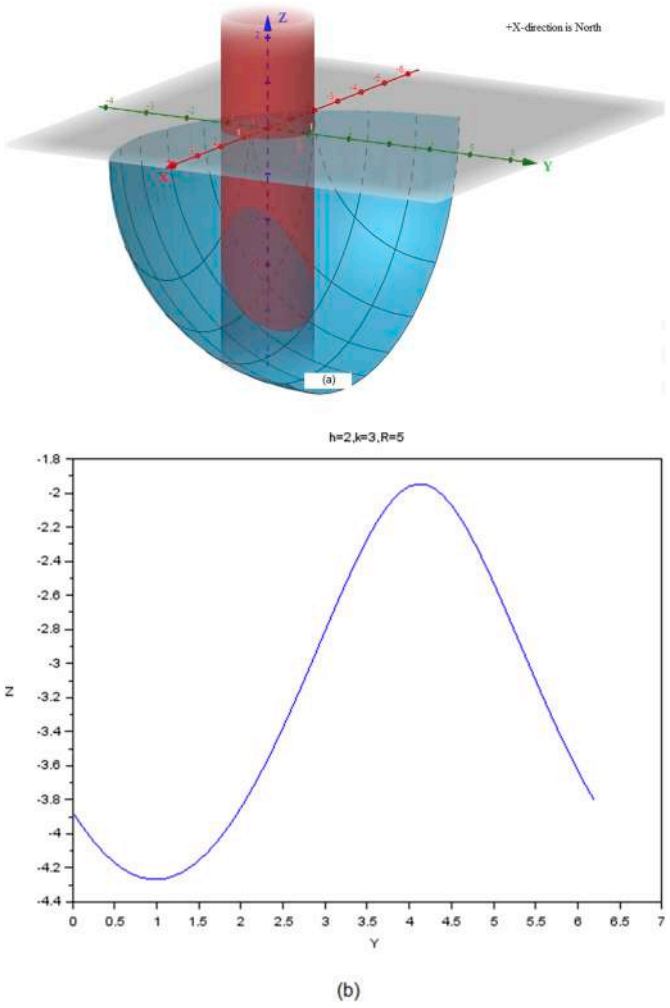

Fig. 17. (a): Intersection between a vertical drill core and a listric surface that is part of a sphere. **(b):** Unrolled image of the fault as shown in the previous subfigure. See Section 2.5.3.2 for details.

$$z(\varphi') = \frac{(\cos\varphi' - h)^2 + (\sin\varphi' - k)^2}{a} \tag{59}$$

Fig. 18(a) shows a part of a paraboloid with $h = 2$, $k = 3$ and $a = 10$, and the cylinder with unit circular cross-section. Fig. 18(b) shows the corresponding unrolled image that shows the listric fault plane. This figures was produced by utilizing the MATLAB programming as shown in Appendix 8: Ellipsoidal surface. Consider the surface of the fault to be a part of a ellipsoid:

$$\frac{(x-h)^2}{a^2} + \frac{(y-k)^2}{b^2} + \frac{z^2}{c^2} = 1 \tag{60}$$

with the centre at $(h, k, 0)$. The equation of the line of intersection between the listric fault surface and the drill core surface, from eqns (1), (2) and (60):

$$z(\varphi') = c\left[1 - \frac{(\cos\varphi' - h)^2}{a^2} - \frac{(\sin\varphi' - k)^2}{b^2}\right]^{1/2} \tag{61}$$

Fig. 19(a) shows a part of an ellipsoid with $h = 2, k = 1, a = 4, b = 3$ and $c = 2$ and the cylinder with unit circular cross-section. Fig. 19(b) shows the corresponding unrolled image. This figure utilizes the MATLAB programming as shown in Appendix 8. As expected, geometrical differences in listric faults (Figs. 17a, 18a and 19a) planes are reflected (subtly) in their unrolled images (Figs. 17b, 18b and 19b). Type-2 listric

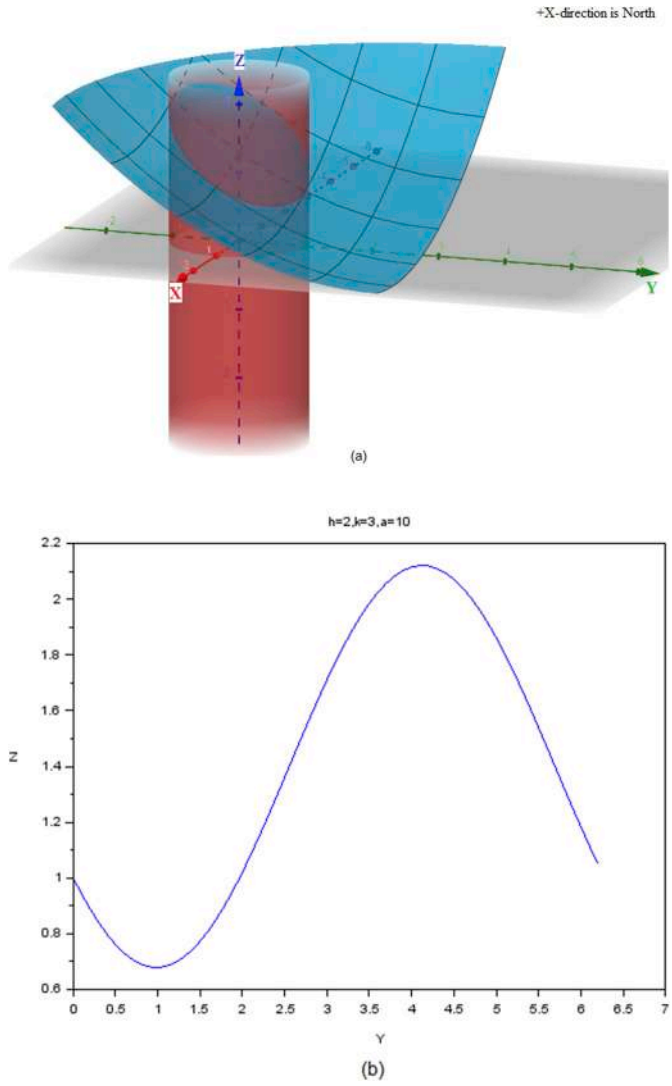

Fig. 18. (a): Intersection of a vertical drill core with a listric surface that is part of a paraboloid. **(b):** Unrolled image of the fault as shown in the previous subfigure. See Section 2.5.3.3 for details.

faults Mukherjee and Chakraborty (2020) consider a special type of listric fault as the type-2 one. In this case, the fault plane is non-spherical that intersects an imaginary horizontal plane as a straight line. Chakravarthi (2011) refers to a similar fault plane in his geophysical studies.

The equation of such a fault is:

$$\frac{(y-k)^2}{a^2} + \frac{(z)^2}{b^2} = 1 \tag{62}$$

The ellipse has a centre at $(k, 0)$ in the YZ plane. The equation of the line of intersection between the listric fault plane and the cylinder, deduced from eqns (1), (2) and (62):

$$z(\varphi') = b\left[1 - \frac{(\sin\varphi' - k)^2}{a^2}\right]^{1/2} \tag{63}$$

Fig. 20(a) shows a part of an type-2 fault with $k = 3$, $a = 5$ and $b = 2$ and the cylinder with unit circular cross-section. Fig. 20(b) shows the unrolled image of the listric fault plane. Fig. 20(b) was produced by writing a MATLAB programme (Appendix 10). Comparing this image with the unrolled image of a fault plane which is not a Type-2 listric

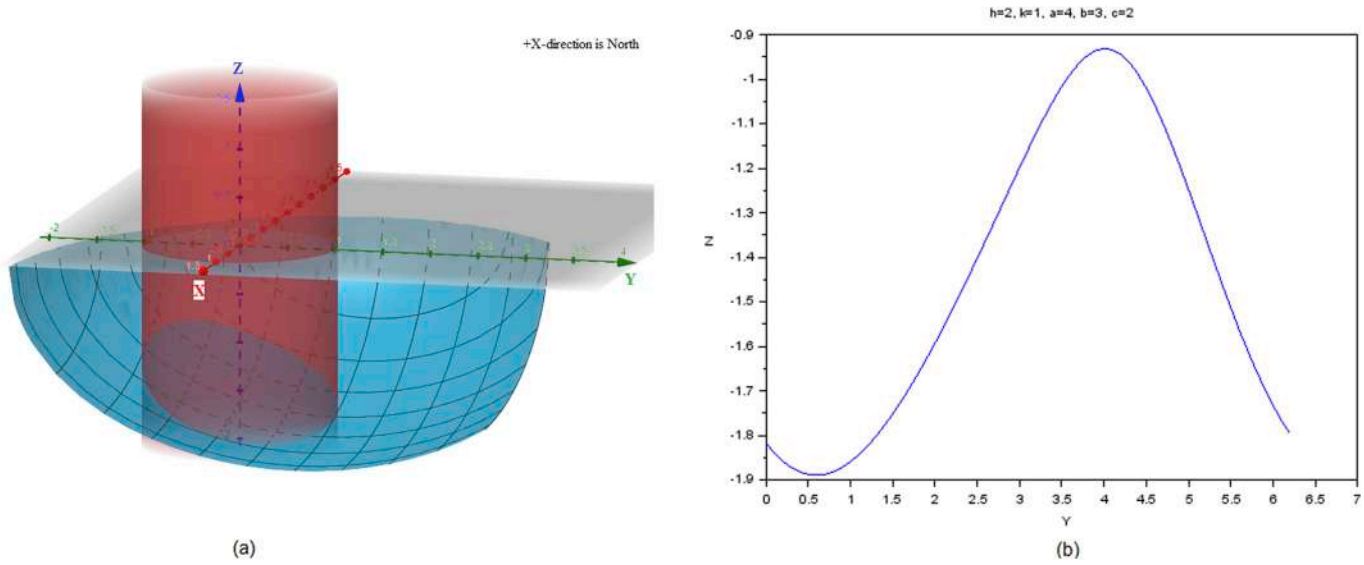

Fig. 19. (a): Intersection between a vertical drill core and a listric surface that is part of an ellipsoid. **(b):** Unrolled image of the fault as shown in the previous subfigure. See Section 2.5.3.4 for details.

fault (e.g., Fig. 19(b)), we can infer that it is not possible to separate the two types of listric faults solely based on their unrolled images.

2.5.4. Angular unconformities

We discuss two possible drilling scenarios over an angular unconformity, and understand there can be several other possibilities. Fig. 21(a) shows an angular unconformity as a combination of underlying inclined and overlying horizontal planes. Using the MATLAB programming (Appendix 1), Fig. 21(b) shows the corresponding unrolled image showing those planes.

Fig. 22(a) shows an angular unconformity as a combination of underlying folded layers and overlying horizontal planes. Drilling in this case is made on the hinge region of the folded layers below the unconformity. Fig. 22(b) shows the corresponding unrolled image. This figure utilizes the MATLAB programming shown in Appendix 4. In case drilling were made away from the hinge region of the underlying fold so that the drill would have cut only the limbs of the fold, one would get the unrolled image resembling Fig. 21(b).

3. General discussions

A rigorous deduction of different ideal structures in unrolled images have remained unclear so far, which this article addresses. In all cases we consider that the geological structures fully cut across the drill wells. However, there are also natural cases that a plane can cut the core partially (Fig. 19.30 in Ellis and Singer, 2008, Fig. 3(c) in Wenning et al., 2017).

How borehole breakouts and induced fractures would appear in image logs have been studied to some extent (e.g., Figs. 14 and 16, respectively, in Davatzes and Hickman, 2010) and we avoid its discussion here. Geological structures can have enormous morphological variations. The situation can be further complicated in structurally multi-deformed terrains. For example, rocks displaying angular unconformity can subsequently fold and therefore simple situations (e.g., Figs. 21a and 22a) might modify.

A natural slump fold, such as the image log presented in Fig. 26 of Slatt and Davis, 2010, or any other polyclinal fold has complicated/

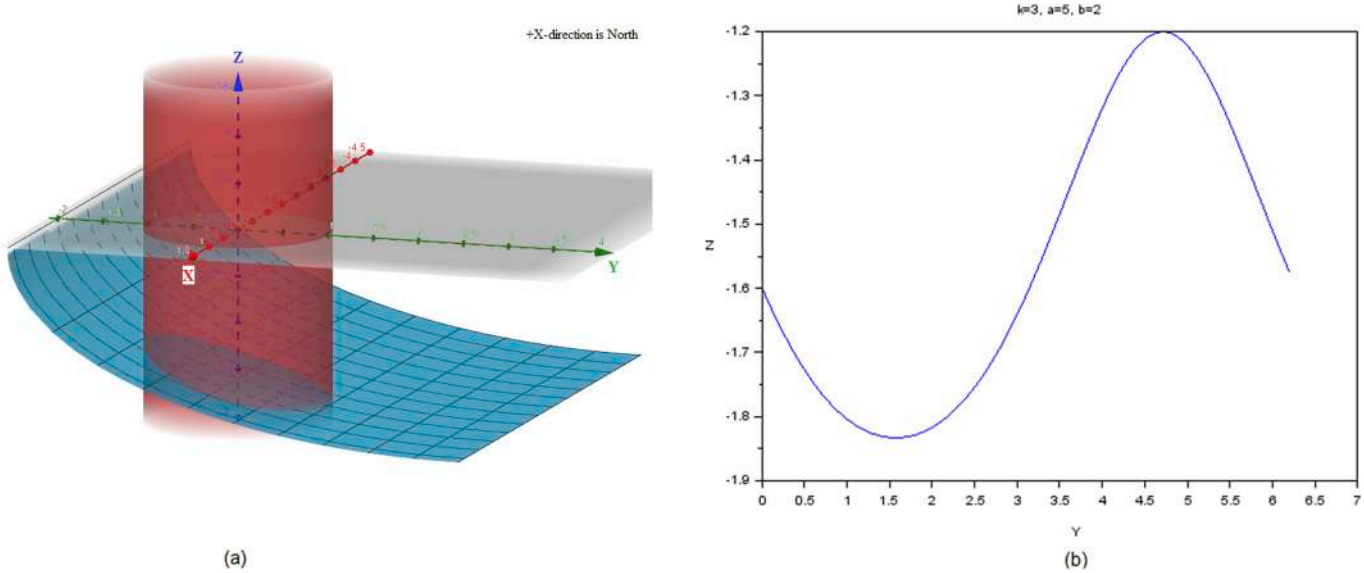

Fig. 20. (a): Intersection between a vertical drill core and a type-2 listric fault. **(b):** Unrolled image of the fault as shown in the previous subfigure. See Section 2.5.3.5 for details.

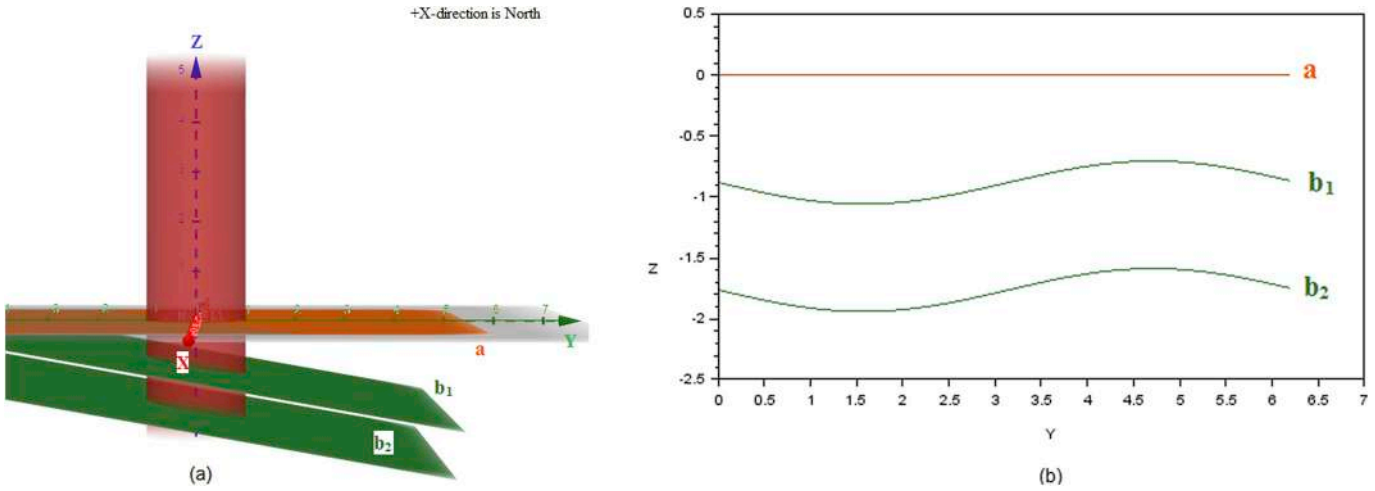

Fig. 21. (a): Vertical drilling that cuts an angular unconformity. **(b):** Unrolled image representing the planes above and below an angular unconformity. See Section 2.5.4 for details.

irregular geometry. To our knowledge, so far no research article has produced 3D equations for such folds. Thus, generating their ideal unrolled image is not possible at present as per the work-flow presented in this article.

Dipping planes can be irregular while overall being a planar surface, therefore some deviation from ideal sinusoidal geometry is possible (e.g., Fig. 15(a) in Barton and Moos, 2010, Fig. 31 of Cao et al., 2018).

The ideal unrolled images shown for the dipping planar and curviplanar planes for different structures in this article would therefore vary to a large extent when the unrolled images of the real drill cores are considered. Nevertheless, this article provides a guideline for their ideal representation, and will be useful for the novices to work with unrolled images of drill cores (e.g., the fold in Fig. 7(c) of Wenning et al., 2017). Further, one can test how other structures, of known or idealized 3D geometries, will look like in unrolled images following this article.

It is not possible to identify accurate structures just based on the unrolled images of drill cores. One would require additional information, such as possibly the drill core itself, to understand the structures. For example, Fig. 8(a) considers intersecting fractures and Fig. 8(b) is the unrolled image. Note that the same unrolled images would appear if one of those two planes is a bedding plane and the other is a fracture plane. For this reason, one need to also take help of the drill cores, and then mark in the unrolled image different colours for different planes. The most common convention is to mark bedding planes by red colour, and fractures by green colour (e.g., Fig. 15 of Hansen and Buczak, 2010). In a similar way, finding straight horizontal lines across which few curved lines terminate (e.g., Fig. 22b) in an unrolled image does not guarantee the structure to be an unconformity. It can also be a case of inclined fracture planes that abut against horizontal planes (e.g., Fig. 7 of Mattioni et al., 2010).

Identifying fault planes based on drill cores could be easy as faults sometimes contain gouge and/or breccias and slipped markers that can be documented in the drill cores themselves (Lorenz and Cooper, 2018). Also, one needs to get trained with the fault rock texture that is displayed typically in image logs (e.g., Fig. 7 of Davatzes and Hickman, 2010).

In few cases, the reader can make out now how other structures can look like in an unrolled image. For example, disconformities, nonconformities and paraconformities have parallel and horizontal layers above and below them. Making vertical drill cores out of them followed by producing unrolled images will yield ideally horizontal parallel straight lines. These obvious cases are not shown separately in this work. The presented graphs may not match 100% with real planar structures as the latter can have (minor) irregularities in geometries. On the other hand, we considered perfectly planar structures in few cases (fractures in Section 2.5.1 and unconformities in Section 2.5.4).

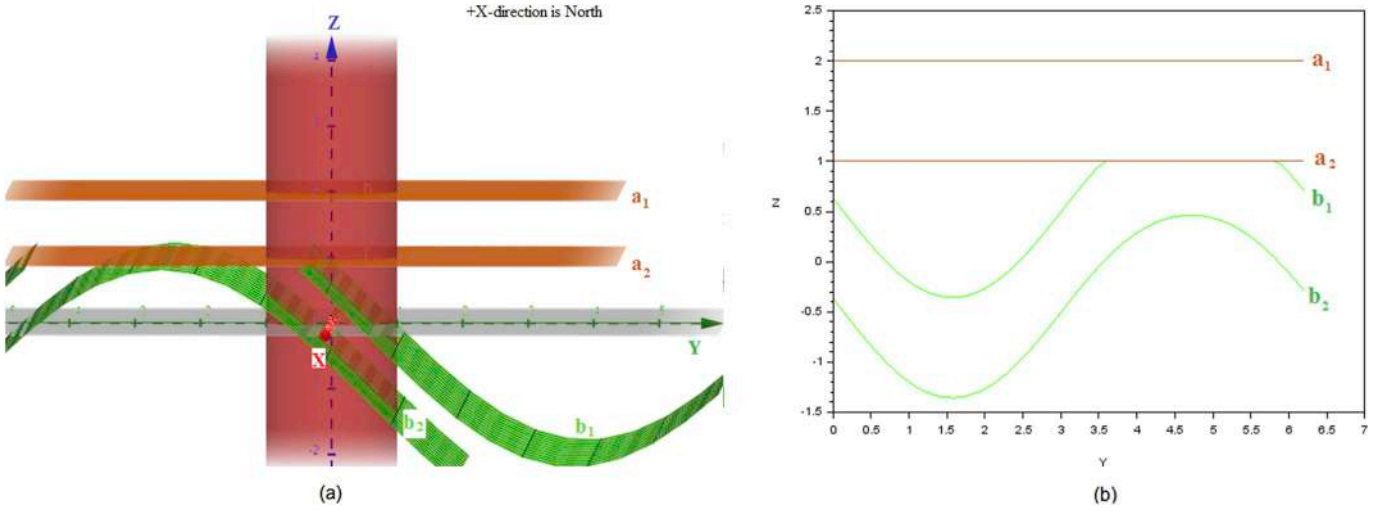

Fig. 22. (a): Vertical drilling that cuts an angular unconformity. **(b):** Unrolled image representing the folded planes below the angular unconformity and the horizontal planes above it. See Section 2.5.4 for details.

How different structures would appear in an unrolled image when the drill core is non-cylindrical (e.g., Fig. 6 in Cornet, 2013) remains a matter of future research.

Credit author statement

MC received the idea and elaborated the maths while and after attending SM's instructions for her compulsory course: "Structural Geology Stratigraphy" (GS 416) as an M. Sc. 1st Yr Applied Geophysics student in 2019. SM wrote this article. Both MC and SM revised the article.

Acknowledgements

SM was supported by the flexible CPDA grant of IIT Bombay. Positive editorial handling by Adam Bumby and review comments from Dr. Xiaojun Feng and an anonymous person.

Appendix A

1. For Fig. 3(a–i):

For circular cross-section (also used for Figs. 8(b), 10(b) and 21(b)):

```
y = 0:0.1:2*pi %from equation (12), the Y-axis will correspond to the azimuths in the cylindrical core.
theta = 60*pi/180 %dip of the plane.
phi = 270*pi/180 %dip direction of the plane.
for i = 1:length(y).
  z(i)=(sin (phi)*sin (y(i))-cos (phi)*cos (y(i))-1)*tan (theta) % refer to eqn (32).
end.
plot (y,z,'b')
xlabel ('Y')
ylabel ('Z')
```

For elliptical cross-section:

```
function y = f(x) %x represents azimuth and y is the radius as a function of the azimuth.
  A = 1 %α as given in eqn (6).
  B = 3/2 %β as given in eqn (6).
  y = A*B/sqrt (B*B*cos(x)*cos(x)+A*A*sin(x)*sin(x))
endfunction.
phi = 0:0.1:2*pi %azimuths of the cylinder.
theta = 60*pi/180 %dip of plane.
Phi = 315*pi/180 %dip direction of the plane.
for i = 1:length (phi).
  r(i) = f (phi(i))
  y(i) = intg (0,phi(i),f) %refer to eqn (10).
  z(i)=(sin (Phi)*r(i)*sin (phi(i))-cos (Phi)*r(i)*cos (phi(i)))*tan (theta).
end.
plot (y,z,'r')
xlabel ('Y')
ylabel ('Z')
title ('Dip direction = 315, Dip = 60')
```

2. For Figs. 5(b), 7(b) and 9(b) and 11(b):

```
y = 0:0.1:2*pi.
theta = 40*pi/180.
phi = 90*pi/180.
lambda = 45*pi/180 %plunge of core.
Phi = 60*pi/180 %trend of core.
a = cos (phi)*cos (Phi)*sin (lambda)+sin (phi)*sin (Phi)*sin (lambda)+cos (lambda)/tan (theta).
b = cos (phi)*sin (Phi)-sin (phi)*cos (Phi).
c = sin (lambda)/tan (theta)-cos (phi)*cos (Phi)*cos (lambda)-sin (phi)*sin (Phi)*cos (lambda).
for i = 1:length(y).
  z(i) = -(a*cos (y(i))+b*sin (y(i)))/c %for a, b and c refer to eqn (40).
end.
plot (y,z,'b')
xlabel ('Y')
ylabel ('Z')
```

3. For Fig. 12:

```
x = −3:0.1:3.
plot (x, 1.5*cos (2*(x-0.5))) % a = 1.5 b = 2 c = 0.5.
x_location = "origin";
y_location = "origin";
title ('Plot for z = a cos b (y - c)')
```

4. For Figs. 13(b), 14(b) and 22(b):

```
phi = 0:0.1:2*pi.
b = 2.
c = 0.5.
for i = 1:length (phi).
  y(i) = phi(i).
  z(i) = cos (b*(sin (phi(i))-c)) % refer to eqn (43).
end.
plot (y,z,'g')
```

5. For Fig. 15(b):

```
phi = 0:0.1:2*pi.
for i = 1:length (phi).
  y(i) = phi(i).
  z(i) = cos (0.5*cos (phi(i)))+cos (3*(sin (phi(i)))) %refer to eqn (49).
end.
plot (y,z).
title ('Type 1 fold')
xlabel ('Y')
ylabel ('Z')
```

6. For Fig. 16(a′), (b′) and 16(c′):

```
phi = 0:0.1:2*pi.
for i = 1:length (phi).
  y(i) = phi(i).
  z(i) = cos (2*(sin (phi(i)))+0.5 + cos (cos (phi(i))-2)) %refer to eqn (53).
end.
plot (y,z).
title ('Type 2 fold')
xlabel ('Y')
ylabel ('Z')
```

7. For Fig. 17(b):

```
phi = 0:0.1:2*pi.
h = 2.
k = 3.
R = 5.
for i = 1:length (phi).
  y(i) = phi(i).
  z(i) = -sqrt (R**2-(cos (phi(i))-h)**2-(sin (phi(i))-k)**2)%refer to eqn (57).
end.
```

```
plot (y,z).
title ('h = 2,k = 3,R = 5')
```

8. For Fig. 18(b):

```
phi = 0:0.1:2*pi.
h = 2.
k = 3.
a = 10.
for i = 1:length (phi).
  y(i) = phi(i).
  z(i)=((cos (phi(i))-h)**2+(sin (phi(i))-k)**2)/a %refer to eqn (59).
end.
plot (y,z).
title ('h = 2,k = 3,a = 10')
```

9. For Fig. 19(b):

```
phi = 0:0.1:2*pi.
Alpha = 2.
Beta = 1.
a = 4.
b = 3.
c = 2.
for i = 1:length (phi).
  y(i) = phi(i).
  z(i) = -c*sqrt (1-((cos (phi(i))-Alpha)**2)/(a**2)-((sin (phi(i))-
  Beta)**2)/(b**2)) %refer to eqn (61).
end.
plot (y,z).
title ('h = 2, k = 1, a = 4, b = 3, c = 2')
```

10. For Fig. 20(b):

```
phi = 0:0.1:2*pi.
Beta = 3.
a = 5.
b = 2.
for i = 1:length (phi).
  y(i) = phi(i).
  z(i) = -b*sqrt (1-((sin (phi(i))-Beta)**2)/(a**2)) %refer to eqn (63).
end.
plot (y,z).
title ('k = 3, a = 5, b = 2')
```

Appendix B. Supplementary data

Supplementary data to this article can be found online at https://doi.org/10.1016/j.marpetgeo.2020.104241.

References

Abzalov, M., 2016. Applied Mining Geology. Springer, 978-3-319-39263-9pp. 50–53.

Al-Sit, W.T., 2015. Automatic Feature Detection and Interpretation in Borehole Data. Ph.D. thesis. University of Liverpool, pp. 1–120.

Arfken George, B., Weber Hans, J., Harris Frank, E., 2007. Mathematical Methods for Physicists. Elsevier, Berlin, 978-0-12-384654-9pp. 139–142.

Barton, C., Moos, D., 2010. Geomechanical wellbore imaging: key to managing the asset life cycle. In: Poppelreiter, M., Garcıa- Carballido, C., Kraaijveld, M. (Eds.), Dipmeter and Borehole Image Log Technology: AAPG Memoir 92, pp. 81–112.

Bastida, F., Aller, J., Bobillo-Ares, N.C., Toimil, N.C., 2005. Fold geometry: a basis for their kinematic analysis. Earth Sci. Rev. 70, 129–164.

Benjemaa, M., Glinsky-Olivier, N., Cruz-Atienza, V.M., Virieux, J., Piperno, S., 2007. Dynamic non-planar crack rupture by a finite volume method. Geophys. J. Int. 171, 271–285.

Blenkinsop, T.G., Doyle, M.G., 2010. A method for measuring the orientations of planar structures in cut core. Journal of Structural Geology 32, 741–745.

Cao, M., Deng, Z., Rai, L., Teng, S., Zhao, M., Collier, M., 2018. Generating panoramic unfolded image from borehole video acquired through APBT. Multimed. Tools Appl. 77, 25149–25179.

Chakravarthi, V., 2011. Automatic gravity optimization of 2.5D strike listric fault sources with analytically defined fault planes and depth-dependent density. Geophysics 76.

Cornet, J., 2013. Fracture Detection and Analysis on Wellbore Images. Norwegian University of Science and Technology Masters thesis.

Davatzes, N.C., Hickman, S.H., 2010. Stress, fracture, and fluid-flow analysis using aoustic and electrical image logs in hot fractured granites of the Coso geothermal field, California, U.S.A. In: Poppelreiter, M., Garcıa-Carballido, C., Kraaijveld, M. (Eds.), Dipmeter and Borehole Image Log Technology: AAPG Memoir 92, pp. 259–293.

Dasgupta, T., Dasgupta, S., Mukherjee, S., 2019. Image log interpretation of geomechanical issues. In: Mukherjee, S. (Ed.), Teaching Methodologies in Structural Geology and Tectonics. Springer, pp. 237–251.

Ellis, D.V., Singer, J.M., 2008. second ed. Well Logging for Earth Scientists, vol. 564 Springer978-1-4020-3738-2.

Ellis, P.G., McClay, K.R., 1988. Listric extensional fault systems - results of analogue model experiments. Basin Res. 1, 55–70.

Ghosh, S.K., 1993. Structural Geology: Fundamentals and Modern Developments. Pergamon Press, Oxford, 0 08 0 41879 1pp. 237–240.

Hansen, B., Buczak, J., 2010. Making interpretable images from image logs. In: Poppelreiter, M., Garcıa-Carballido, C., Kraaijveld, M. (Eds.), Dipmeter and Borehole Image Log Technology: AAPG Memoir 92, pp. 51–66.

Hinman, M., 1993. A Lotus 1-2-3 diamond drillhole structural manipulation spreadsheet: Drillcore structural data generation. Comput. Geosci. 19, 343–354.

Johnson, J.D., 1985. Interpretation of refoiding and asymmetric folds using vergence concepts in drilicore. J. Struct. Geol. 7, 317–326.

Laing, W.P., 1977. Structural interpretation of drill core from folded and cleaved rocks. Econ. Geol. 72, 671–685.

Lau, J.S.O., 1983. The determination of true orientations of fractures in rock cores. Can. Geotech. J. 20, 221–227.

Liu, H., 2017. second ed. Principles and Applications of Well Logging, vol. 43 Springer978-3-662-54976-6.

Lohr, T., Krawczyk, C.M., Oncken, O., Tanner, D.C., 2008. Evolution of a fault surface from 3D attribute analysis and displacement measurements. J. Struct. Geol. 30, 690–700.

Lorenz, J.C., Cooper, S.P., 2018. Atlas of Natural and Induced Fractures in Core. Wiley Blackwell, Hoboken, 9781119160007pp. 1–305.

Madariaga, R., 1976. Dynamics of an expanding circular fault. Bull. Seismol. Soc. Am. 66, 639–666.

Marjoribanks, R., 2012. Geological Methods in Mineral Exploration and Mining. In: Second Edition. Springer, pp. 106 ISBN: 978-3-540-74370-5.

Marshak, S., Mitra, G., 1988. Basic Methods of Structural Geology. Prentice Hall.

Mattioni, L., Chauveau, A., Fonta, O., Ryabchenko, V., Sokolov, E., Mukhametzyanov, R., Shlionkin, S., Zereninov, V., Bobb, I., 2010. A 3-D fracture model of the Kuyumba oil field (eastern Siberia) reflecting the clay and bed thickness-related fracture-density variations of its dolomite reservoir. In: Poppelreiter, M., Garcıa-Caballido, C., Kraaijveld, M. (Eds.), Dipmeter and Borehole Image Log Technology: AAPG Memoir 92, pp. 211–227.

McHone, J.G., Anderson, D.L., Beutel, E.K., Fialco, Y.A., 2005. Giant dykes, rifts, flood basalts, and plate tectonics: A contention of mantle models. In: In: Foulger, G.R., Natland, J.H., Presnall, D.C., Anderson, D.L. (Eds.), Plates, Plumes Paradigms, vol. 388. Geol Soc Am Spec Pap, pp. 401–420.

Morin, M.L., 2017. Natural and Drilling Induced Fractures in the Grosmont Formation, Alberta: Implications for the State of Stress. Master of Science Thesis. University of Alberta, pp. 1–108.

Mukherjee, S., Chakraborty, M., 2020. 3-D slip analyses of listric faults with ideal geometries. Mar. Pet. Geol. 112, 104092.

Mukherjee, S., Tayade, L., 2019. Kinematic analyses of brittle roto-translational planar and listric faults based on various rotational to translational velocities of the faulted blocks. Mar. Pet. Geol. 107, 326–333.

Oakley, D.O.S., 2017. Fault-propagation Fold Kinematics and Deformation Rates in theNorth Canterbury Fold and Thrust Belt, South Island, New Zealand. The Pennsylvania State University, pp. 1–327 Ph.D. thesis.

Paulsen, T.S., Jarrard, R.D., Wilson, T.J., 2002. A simple method for orienting drill core by correlating features in whole-core scans and oriented borehole wall imagery. J. Struct. Geol. 24, 1233–1238.

Quiniou, T., Selmaoui, N., Laporte-Magoni, C., Allenbach, M., 2007. Calculation of bedding angles inclination from drill core digital images. In: MVA2007 IAPR Conference on Machine Vision Applications, May 16-18, Tokyo.

Ritz, E.M., 2013. Mechanical Behavior of Non-planar Faults: Numerical Experiments and Field Observations. Stanford University, pp. 1–156 Ph.D. thesis.

Schultz, R.A., 1987. Mechanics of Curved Strike-Slip Faults. Ph.D. thesis. Purdue University, pp. 1–142.

Schultz, R.A., 1992. Mechanics of curved slip surfaces in rock. Eng. Anal. Bound. Elem. 10, 148–154.

Scott, R.J., Berry, R.F., 2004. A new method for obtaining and quantifying the reliability of structural data from axially-oriented drill core using a fabric of known orientation. J. Struct. Geol. 26, 643–658.

Scott, R.J., Selley, D., 2004. Measurement of fold axes in drill core. J. Struct. Geol. 26, 637–642.

Shigematsu, N., Otsubo, M., Fujimoto, K., Tanaka, N., 2014. Orienting drill core using borehole-wall image correlation analysis. J. Struct. Geol. 67, 293–299.

Sikorski, R.I., 1991. A diagram for interpreting orientation data for planar features in core. J. Struct. Geol. 13, 1085–1089.

Slatt, R.M., Davis, R.J., 2010. Calibrating borehole image and dipmeter logswith outcrops and behind-outcrop cores: Case studies and applications to deep-water deposits. In: Poppelreiter, M., Garcıa-Carballido, C., Kraaijveld, M. (Eds.), Dipmeter and Borehole Image Log Technology: AAPG Memoir 92, pp. 167–194.

Tiwari, S., Mishra, S., Sriharipraśad, G., Vyas, D., Warhade, A., Nikalje, D., Bartakke, V., Tembhurnikar, P., Roy, S., 2017. High Resolution Core Scan Facility at BGRL-MoES, Karad, India. J. Geol. Soc. India 90, 795–797.

van der Pluijm, Marshak, S., 2004. Earth Structures: an Introduction to Structural Geology and Tectonics. W.W. Norton Company, New York, 0-393-92467-Xpp. 145.

Wenning, Q., Berthet, C.T., Ask, M., Zappone, A., Rosberg, J.-E., Almqvist, B.S.G., 2017. Image log analysis of in situ stress orientation, breakout growth, and natural geologic structures to 2.5 km depth in central Scandinavian Caledonides: Results from the COSC-1 borehole. J. Geophys. Res. Solid Earth 122, 3999–4019.

Wriggers, P., Vu Van, T., Stein, E., 1990. Finite element formulation of large deformation impact-contact problems with friction. Comput. Struct. 37, 319–331.

Yamada, Y., McClay, K., 2003. Application of geometric models to inverted listric fault systems in sandbox experiments. Paper 2: insights for possible along strike migration of material during 3D hanging wall deformation. J. Struct. Geol. 25, 1331–1336.

Yeh, E.-C., Sone, H., Nakaya, E., Ian, K.-H., Song, S.R., Hung, J.-H., Lin, W., Hirono, T., Wang, C.-Y., Ma, K.-F., Soh, W., Kinoshita, M., 2007. Core Description and Characteristics of Fault Zones from Hole-A of the Taiwan Chelungpu-Fault Drilling Project. Terr. Atmos. Ocean. Sci. 18, 327–357.

Zhang, X., Zhang, W., Xiao, X., 2014. Rapid detection of bedding boundaries based on borehole images. Comput. Model. N. Technol. 18, 207–211.

Zimmer, P.W., 1963. Orientation of small diameter drillcore. Econ. Geol. 58, 1313–1325.

Zosel, A., 2015. Development and Application of a Method for Unwrapping Single Images of Cylindrical Objects. Montana Tech of the University of Montana, pp. 1–141. Thesis. pp, Graduate Theses Non-Theses. 24. http://digitalcommons.mtech.edu/gradrsch/24,sch/24.